

1 **Decoding spatiotemporal gene expression of the developing human spinal cord and**
2 **implications for ependymoma origin**

3
4 Xiaofei Li ^{1*}, Zaneta Andrusivova ², Paulo Czarnecki ^{2,3}, Christoffer Mattsson Langseth ⁴,
5 Alma Andersson², Yang Liu^{1,5}, Daniel Gyllborg ⁴, Emelie Braun ⁶, Ludvig Larsson ², Lijuan
6 Hu ⁶, Zhanna Alekseenko ^{1,7}, Hower Lee⁴, Christophe Avenel ^{8,9}, Helena Kopp Kallner ¹⁰,
7 Elisabet Åkesson ^{1,11}, Igor Adameyko ^{12,13}, Mats Nilsson ⁴, Sten Linnarsson ⁶, Joakim
8 Lundeberg ², Erik Sundström ^{1*}

9
10 ¹Division of Neurogeriatrics, Department of Neurobiology, Care Sciences and Society,
11 Karolinska Institutet, Stockholm, Sweden

12 ²Science for Life Laboratory, Department of Gene Technology, KTH Royal Institute of
13 Technology, Stockholm, Sweden

14 ³Science for Life Laboratory, Department of Biochemistry and Biophysics,
15 National Bioinformatics Infrastructure Sweden, Stockholm University, Stockholm, Sweden

16 ⁴Science for Life Laboratory, Department of Biochemistry and Biophysics, Stockholm
17 University, Stockholm, Sweden

18 ⁵China National Clinical Research Center for Neurological Diseases, Beijing Tiantan
19 Hospital, Capital Medical University, Beijing, China

20 ⁶Division of Molecular Neurobiology, Department of Medical Biochemistry and Biophysics,
21 Karolinska Institutet, Stockholm, Sweden

22 ⁷Department of Cell and Molecular Biology, Karolinska Institutet, Stockholm, Sweden

23 ⁸Department of Information Technology, Uppsala University, Uppsala, Sweden

24 ⁹BioImage Informatics Facility, Science for Life Laboratory, SciLifeLab, Sweden

25 ¹⁰Department of Clinical Sciences, Danderyd Hospital, Stockholm, Sweden

26 ¹¹R&D Unit, Stockholms Sjukhem, Stockholm, Sweden

27 ¹²Department of Physiology and Pharmacology, Karolinska Institutet, Stockholm, Sweden

28 ¹³Department of Neuroimmunology, Center for Brain Research, Medical University of
29 Vienna, Vienna, Austria

30 *Correspondence: xiaofei.li@ki.se (X.L.), erik.sundstrom@ki.se (E.S.)

31
32
33

34 **Abstract**

35 The human spinal cord contains diverse cell types, governed by a series of spatiotemporal
36 events for tissue assembly and functions. However, the spatiotemporal regulation of cell fate
37 specification in the human developing spinal cord remains largely unknown. Single-cell RNA
38 sequencing and spatial transcriptomics techniques have advanced the understanding of human
39 organ development considerably. By performing integrated analysis of single-cell and spatial
40 multi-omics methods, we created a comprehensive developmental cell atlas of the first
41 trimester human spinal cord. Our data revealed that the cell fate commitment of neural
42 progenitor cells and their spatial positioning are spatiotemporally regulated by specific gene
43 sets. Beyond this resource, we unexpectedly discovered unique events in human spinal cord
44 development compared to rodents, including earlier quiescence of active neural stem cells,
45 different regulation of stem cell differentiation, and distinct spatiotemporal genetic regulations
46 of cell fate choices. In addition, using our atlas we identified specific gene expression in cancer
47 stem cells in ependymomas. Thus, we demonstrate spatiotemporal genetic regulation of human
48 spinal cord development as well as its potential to understand novel disease mechanisms and
49 to inspire new therapies.

50

51

52

53

54

55

56

57

58

59 **Main**

60 The spinal cord comprises the caudal region of the central nervous system (CNS) and is
61 responsible for conveying and processing motor and sensory information between the brain
62 and the periphery, as well as for elaborating reflexes. During spinal cord development, neural
63 stem and progenitor cells (NPCs) in the ventricular zone, surrounding the nascent central canal,
64 are committed to their respective cell fates governed by gradients of dorsal and ventral
65 morphogens¹. Consequently, different transcription factors (TFs) along the dorsal-ventral (DV)
66 axis are activated, resulting in spatially segregated progenitor domains. In rodents, domain-
67 specific NPCs temporally undergo cell fate specification, first generating neurons, then glia.
68 These differentiated neural cells migrate from their origin to their final locations in the spinal
69 cord and engage in distinct circuits ¹.

70

71 It is however, not known to what extent this knowledge can be translated to humans. It is
72 generally believed that during the first trimester of human pregnancy, most of the human
73 (h)NPCs are highly proliferative in preparation for neurogenesis and gliogenesis. Therefore,
74 cell therapy approaches such as stem cell therapies for neurotrauma and degenerative diseases,
75 usually obtain hNPCs from the first trimester, thus more likely to acquire active and neuron-
76 fate-committed NPCs. Current studies, however, showed that hNPCs derived from early
77 development exhibit either robust glial differentiation² or little differentiation ³, suggesting that
78 besides the impacts of microenvironment, deciphering the intrinsic genetic regulation for cell
79 fate commitment of hNPCs is necessary to achieve better efficiency of such therapies.
80 Furthermore, impaired neurodevelopment, pediatric tumorigenesis and neurodevelopmental
81 disorders are highly related. Therefore, better understanding of the cell fate commitment of
82 hNPCs in the developing spinal cord can provide insights into human developmental biology,
83 future regenerative strategies and potential pediatric cancer treatment.

84

85 Single-cell RNA sequencing (scRNA-seq) and spatial transcriptomics (ST) have provided
86 high-throughput and spatially resolved analysis of spatiotemporal gene expression during
87 human prenatal development ⁴. Furthermore, a high-throughput and multiplex *in situ*
88 hybridization method, hybridization-based *in situ* sequencing (HybISS) has recently been
89 developed for single RNA molecule localization of large gene panels with single-cell resolution
90 within human tissue for data validation ^{4,5}. Combining all these methods can largely reduce the
91 limitations of individual techniques, facilitate unbiased cell type annotation, and allow high
92 resolution spatiotemporal mapping of the developing human spinal cord. Two recent studies
93 used scRNA-seq on human developing spinal cord and revealed the appearance of different
94 neural cell types ^{6,7}. However, the genetic regulation of the commitment of homogenous hNPCs
95 to heterogenous neuronal and glial fates *in vivo* is still unclear. Furthermore, although neural
96 patterning associated with transient spatial distribution of neural cells during human
97 development is well-known ^{7,8}, how such events result in spatially restricted heterogenous
98 neurons and glia is still not well studied in human. In addition, while the use of transgenic
99 animals during the last two decades has provided detailed mechanisms of the rodent spinal cord
100 development, it is unclear whether there are unique features of the development of the human
101 spinal cord. In this study, we have analyzed human embryonic and fetal spinal cords covering
102 the entire first trimester, using state-of-the-art scRNA-seq, ST and HybISS, and integrated
103 these datasets with previously reported mouse and human spinal cord datasets for our analysis.
104 Here we provide a comprehensive developmental cell atlas of the human spinal cord, reveal
105 spatiotemporal gene expression and regulation of cell fate commitment, highlight the major
106 differences of cellular and molecular events in human and rodent spinal cord development, and
107 discover novel molecular targets and genetic regulation of pediatric spinal cancer stem cells.

108

109 **Comprehensive atlas of the human developing spinal cord**

110 To investigate the molecular features of the developing human spinal cord, we acquired 16
111 human prenatal spinal cords at post-conception week (W) 5-12 (Supplementary Table 1),
112 covering the first trimester of pregnancy when cell fate specifications in the CNS occur ^{9,10}. We
113 performed scRNA-seq, ST and HybISS to create a developmental cell atlas of the human spinal
114 cord with detailed spatiotemporal gene expression and validation (Fig. 1a, Supplementary
115 Table 1). A total of 159,350 high quality cells across 31 scRNA-seq libraries were analyzed,
116 revealing 47 cell clusters (Extended Data Fig. 1a-b) (16 major cell populations) (Fig. 1b). All
117 major spinal cord neural cell types were represented including NPCs, intermediate neuronal
118 progenitors (INPs), excitatory neurons (ExNs), inhibitory neurons (IbNs), cholinergic neurons
119 (ChNs), astrocytes (ASCs), ependymal cells (EPCs), oligodendrocyte precursor cells (OPCs)
120 and oligodendrocytes (OLs) (Fig. 1b), which this study mainly focused on. Other cell types
121 such as Schwann cells (SWCs), pericytes (PCs), endothelial cells (ENs), vascular capillary
122 endothelial cells (VCLPs) and immune cells (Immune) (e.g., microglia) were also derived
123 during this developmental stage (Fig. 1b). Top marker genes of each cell type and cluster are
124 summarized (Fig. 1c, Extended Data Fig. 1c).

125

126 To define the spatial gene expression and analyze cell type localization independently from
127 scRNA-seq, we used sections of the prenatal spinal cords along the rostral-caudal axis (RC) of
128 representative ages (W5, W8, W9 and W12) for analysis. Clustering analysis of ST data from
129 76 sections resulted in 23 clusters along the RC and DV axis (Extended Data Fig. 2a-b,d), and
130 revealed 12 major cell types (Fig. 1d, Extended Data Fig. 2c). At W5, the cross-sectioned
131 human spinal cord was dominated by NPCs in the ventricular zone. From W8 and onwards,
132 not only neurons but all glial cell types were born (Fig. 1d, Extended Data Fig. 2c). In addition,
133 fewer cell types could be identified in the caudal regions with our clustering approach (e.g.,

134 cluster 0 neurons at W8) compared to the rostral regions, suggesting a possible earlier
135 development in rostral regions (Extended Data Fig. 2c and e). However, we did not obtain
136 obvious differences in gene expression by comparing scRNA-seq data and ST data from
137 different regions along the RC axis, suggesting that the asymmetric development along RC
138 axis could be regulated by secreted factors at protein level. To understand the probability of
139 cell types in different of the human spinal cord, we further integrated scRNA-seq and ST data
140 by using *stereoscope*, a recently developed method for guided decomposition of ST data by
141 using scRNA-seq data as reference ¹¹ to delineate the spatial distribution of cell types defined
142 in the scRNA-seq. (Fig. 1e, Extended Data Fig. 3). We found that the dorsal area was mainly
143 occupied by ExNs and IbNs, while the ventral gray matter was mainly occupied by immature
144 neurons and ChNs from W8 (Fig. 1e). Early born glial cells showed cell type specific spatial
145 distributions, including ASCs in the dorsal ventricular zone and EPCs and OPCs in the ventral
146 ventricular zone (W5 and W8 data in Extended Data Fig. 3). Notably, stereoscope data
147 indicates the relative probability of each cell type in certain spot, rather than an absolute value
148 of cell number quantification. To provide single cell spatial mapping resolution and validation,
149 we performed HybISS ⁵ in adjacent tissue sections to visualize the transcriptome *in situ* using
150 50 selected genes (Supplementary Table 3; Supplementary Figure 1) for major cell type
151 characterization and 224 genes for subtype or cell state characterization (Supplementary Table
152 4; Supplementary Figure 2). The HybISS data were integrated with scRNA-seq data by
153 probabilistic cell typing (pciSeq) ¹², and confirmed the findings revealed by ST (Fig. 1f).
154 Notably, either ST or HybISS was also analyzed independently from scRNA-seq data as
155 validation (more detail below).

156

157 **Heterogenous neural cells in the human developing spinal cord**

158 To validate the major cell populations that we identified with scRNA-seq and ST (Fig. 1 b,d,e),
159 we selected 50 genes matching the markers of each major cell type (Supplementary Figure 1)
160 and performed HybISS on the human spinal cord sections. We observed that in agreement with
161 ST and stereoscope data (Fig. 1d-e), NPCs (*ASCL1*+ *SOX2*+) were the major cell population
162 at W5 and were highly proliferative (*MKI67*+*TOP2A*+), but from W8 the proliferating NPCs
163 were restricted to the ventricular zone (Fig 2a). Different neurons, including ExNs (e.g.
164 *CACN2D1*+), IbNs (e.g. *SCGZ*+ or *NRXN3*+) and ChNs (*ISL1*+ and/or *SLC5A7*+) appeared
165 as early as W5 and were widely distributed throughout the gray matter (i.e. the intermediate
166 zone) at W8 (Fig 2a), in line with our ST data (Fig 1d). We further confirmed early
167 neurogenesis for ExNs (*EBF1*+), IbNs (*PAX2*+) and ChNs (*ISL1*+) by immunohistochemistry
168 (IHC) at W8 (Extended Data Fig 4a-b). A previous study on human developing spinal cord
169 showed that glial cells first appeared at W7-8⁶, equivalent to mouse embryonic day (E) 14-16.
170 However, we observed that all glial cell markers were expressed at W5, in which we found that
171 ASCs (*MSX1*+*GFAP*+) were derived from the dorsal ventricular zone, EPCs
172 (*FOXJ1*+*RFX4*+) were derived from the ventral ventricular zone, and OPCs
173 (*OLIG1*+*OLIG2*+) were derived from pMN domain (Fig 2a). All these glial cell types showed
174 *MKI67* expression, suggesting that gliogenesis continued during the early stage of first
175 trimester from W5-8 on (Fig 2a, Extended Data Fig 4h). These HybISS data were well
176 correlated with ST and stereoscope data (Extended Data Fig 3), and thus validated the
177 observations by ST. We further performed IHC for these newborn glial cell markers at protein
178 level. We observed IHC signals at W5 for both ASCs (*MSX1*+*GFAP*+) and EPCs
179 (*RFX4*+*FOXJ1*+) in the dorsal and ventral area of the spinal cord, respectively, in agreement
180 with our HybISS results (Fig 2 b-c). However, using immunofluorescence we did not observe
181 OPC markers at the protein level (*PDGFRa*+*OLIG2*+) at W5 (Fig 2d) but found clear double-

182 stained cell profiles at W8 (Extended Data Fig. 4d). Our data suggest that NPCs have were
183 committed to glial fate as early as W5 in the developing human spinal cord.

184

185 To further characterize the heterogenous cell types and cell states during human spinal cord
186 development, we analyzed each major neural cell type and revealed their diversity (Fig 2e).
187 These subpopulations or cell states could be distinguished with single or combinatorial markers
188 (Supplementary Figure 2). We then integrated the scRNA-seq analysis with ST to determine
189 their spatial distribution (Extended Data Fig 5). Some neurons exhibited specific spatial
190 distributions, such as IbNs_2 in the dorsal parts and IbNs_6 in ventral parts. Similarly, the early
191 born glial cells showed specific spatial distributions, with EPCs_0 in the dorsal ventricular
192 zone while EPCs_3 were located in the ventral ventricular zone (Extended Data Fig 5). We
193 further validated the regional distribution of subclusters by HybISS. For instance, IbNs_6
194 neurons (*TAL2*+) were found in the ventral spinal cord (Extended Data Fig 5; Extended Data
195 Fig 4i), and IbNs_13 neurons in the dorsal-central spinal cord and exhibited *GPC5*, *DTX1* and
196 *ROR1* expression (Extended Data Fig 5, Extended Data Fig 4i). For glial cells, we found that
197 most OPCs were derived from the ventral spinal cord (Fig 2a, Extended Data Fig 5) and were
198 *PDGFRA*+*OLIG2*+, but there were distinct subtypes, such as OPCs_2 (*PDGFRA*-
199 *OLIG2*+*NKD1*), and OPCs_3 (*EN2*+) (Extended Data Fig 4i; Supplementary Figure 2).
200 However, many clusters of neuronal and glial cell types did not display regionally specific
201 distributions, suggesting that these subclusters not only include cell subpopulations but also
202 transient cell states during development. Indeed, by performing gene ontology analysis on the
203 differentially expressed genes (DEGs) of different neuronal and glial cell populations, the most
204 common results were associated with “neurodevelopment”, “neurogenesis” and “gliogenesis”.
205 Therefore, we focused on how neurogenesis and gliogenesis are regulated by spatiotemporal

206 gene expression during NPC self-renewal, fate commitment and differentiation in the
207 developing human spinal cord.

208

209 **NPCs are committed to neuronal and glial fates during early spinal cord development**

210 In the analysis of neurodevelopment, we first focused on the NPC populations and found 10
211 different clusters in the scRNA-seq dataset (Fig. 2e). The NPCs clusters could be characterized
212 either by a single marker or by combinatorial markers (Extended Data Fig 6a), and they all
213 expressed neural stem cell and radial glial cell markers at mostly high levels, indicating their
214 stem cell properties (Extended Data Fig. 6b). In contrast to the common view that most NPCs
215 proliferate extensively at this stage ¹, we found that more than half of the clusters expressed
216 low levels of active cell cycle genes (S or G-to-M phase) (Extended Data Fig. 6c). Spatial
217 distribution analysis showed that hNPCs were mostly located around the ventricular zone but
218 with a relatively smaller area at later timepoints compared with W5 (Extended Data Fig. 6d).
219 From W9 to 12, hNPCs could be observed in the intermediate and marginal zones, indicating
220 migration of newly differentiated neuronal and glial progenitors (Extended Data Fig. 6d).
221 Interestingly, HybISS data showed that the expression of proliferation markers (*MKI67* and
222 *TOP2A*) substantially decreased in hNPCs, and hNPCs_10 had even disappeared from W9
223 (Extended Data Fig. 6e). In agreement, immunohistochemistry (IHC) showed that many
224 SOX9+ hNPCs did not express KI67 in the W5 human spinal cord, suggesting that a large
225 proportion of hNPCs enter quiescence in early development (Fig. 5a).

226

227 To analyze the starting point of differentiation, we used two different methods for trajectory
228 analysis, scVelo¹³ (Extended Data Fig 7a-b) and URD¹⁴ (Extended Data Fig 7c-e) on the NPC
229 populations. We showed that all NPC populations were highly connected with each other
230 (Extended Data Fig 7a). The proliferative hNPCs (NPCs_5, 7, 9 and 10) changed their fates

231 towards low-proliferating NPC clusters, developed into NPCs_3 and 4, and further into neurons
232 and glia (Extended Data Fig 7b, more details in Fig. 3). By calculating the most significant
233 lineage-associated genes, we found that different genes including TFs were specifically
234 associated with either neuronal or glial lineages (Extended Data Fig 7e), suggesting that most
235 NPCs were genetically regulated for fate commitment into either neurons or glia at W5 in the
236 human developing spinal cord (Extended Data Fig 7c-e). We confirmed these observations by
237 integrating our scRNA-seq dataset with a recent study on early human spinal cord development
238 (from W4 to W7)⁷ (Extended Data Fig 6f). Consistently, we showed that the most proliferative
239 NPC populations (NPCs_5,7,8 and 9) highly expressed MKI67 and TOP2A, while
240 differentiating NPCs (NPCs_3 and 4) expressed specific markers (*EPHA6* and *SULF2* for
241 NPCs_3, *GADD45G* and *DLL3* for NPCs_4) (Extended Data Fig 6g), in line with the DEG
242 results from our own NPC data (Extended Data Fig 6a). By selecting NPCs from the earliest
243 stages in this integrated dataset (W5 in our data and CS12 from the Rayon2021 data), we
244 analyzed the DEGs by comparing non-proliferative NPCs with proliferative NPCs. Performing
245 GO analysis, we found that the neuronal differentiation and neurogenesis were the top
246 suggested biological processes (Extended data Fig 6h), suggesting that non-proliferative
247 hNPCs were involved in differentiation, in line with our trajectory analysis of NPCs.

248

249 **Spatiotemporal gene expression regulates neurogenesis and gliogenesis in the human
250 developing spinal cord**

251 To characterize NPC development into different neuronal and glial populations, we selected
252 the clusters related to NPCs and neurons from the scRNA-seq data for three trajectory analysis
253 by Slingshot, RNA velocity and URD¹⁴⁻¹⁶ (Fig. 3a and e, Extended Data Fig. 8 a-b). Slingshot
254 analysis revealed that NPCs gave rise to different neurons during neurogenesis (Fig. 3a-b;
255 Supplementary Figure 3a-b), with specific gene expression associated with each branch (Fig.

256 3a; Supplementary Figure 3c-d). As shown previously in W8-12, ExNs and IbNs mainly
257 occupied the dorsal horns while ChNs were distributed in the ventral area (Extended Data Fig.
258 3c, Fig. 2a). We validated whether these newborn neurons co-expressed neuronal markers and
259 trajectory-related genes by HybISS and found that at W8 they co-expressed NPC marker genes
260 (*DCC* and *GADD45G*), neuronal-lineage associated genes revealed by trajectory analysis
261 (*CACNA2D1* in ExNs, *NRXN3* in IbNs, *NEFL* in ChNs;) and neuronal markers (*KCNIP4* in
262 ExNs, *ROBO3* in IbNs, *SLC5A7* in ChNs) (enlarged areas shown in Fig. 3b, overview images
263 in Extended Data Fig. 8c). Our results validated that hNPCs co-express specific lineage-
264 associated genes when they are committed into specific neuronal cells.

265

266 As neurons have regionally specific distributions in the spinal cord (i.e. sensory neurons in the
267 dorsal horn and motor neurons in the ventral horn), we wondered whether this spatial
268 distribution of different cell types is not only temporal, but also spatially regulated during
269 neurodevelopment. To this end, we spatially delineated neuronal differentiation, by integrating
270 our scRNA-seq trajectory and ST data. We found that hNPC differentiated into INPs first, then
271 into different functional neurons, and the process was specifically regulated to the spatial
272 distribution of different neurons (Fig. 3c). Furthermore, to validate these spatial trajectory
273 calculations, we developed a method and implemented it as an R package that allowed us to
274 spatially quantify gene expression along the DV axis in the ST dataset, independent from the
275 scRNA-seq data. We found that the most significant temporal lineage-associated genes
276 revealed by scRNA-seq, such as *EBF1* (for ExNs), *PAX2* (for IbNs) and *SLC5A7* (for ChNs)
277 exhibited a biased DV expression in ST analysis, which correlated with the terminally
278 differentiated neuron types (Fig. 3d, Extended Data Fig. 8d). *PBX3* was associated with all
279 three neuronal lineages, thus did not exhibit a specific DV pattern from W8 (Fig. 3d). The
280 results were again confirmed by the gene expression pattern displayed with HybISS (Extended

281 Data Fig. 8c). Therefore, the temporal genetic regulation of human neurogenesis revealed by
282 our scRNA-seq data correlates with spatial positioning of neuronal subtypes in the developing
283 spinal cord, revealed by ST and HybISS.

284

285 To investigate gliogenesis in the human developing spinal cord, we performed similar analysis
286 as above integrating scRNA-seq and ST. We found that all three glial lineages originated from
287 one common NPC subtype (Fig. 3e, Extended Data Fig. 8a-b) and identified the most
288 significant genes associated with the branches of the trajectories, such as *CNTNAP5* for EPCs,
289 *MSX1* for ASCs and *HES6* for OPCs (Fig. 3e, Extended Data Fig. 8b, Supplementary Figure.
290 3e-f). Since the newborn glial cells exhibited certain spatial patterns at W5-9 before migration
291 at W12 (Extended Data Fig. 3), we inferred that the temporal lineage-associated genes could
292 also spatially regulate gliogenesis. Indeed, *MSX1* (in ASCs), *FGFBP3* (in EPCs) and *RGS16*
293 (in OPCs) were spatially expressed in the same area as the newborn glial cells i.e. the *GFAP* +
294 ASCs, *FOXJ1* + EPCs and *OLIG1* + and *OLIG2* + OPCs (Fig. 3f, Extended Data Fig.
295 8c). Integrated trajectory and ST data showed that hNPCs differentiated into glial cells in
296 specific spatial patterns – ASCs in the dorsal, EPCs in the central and OPCs and OLs in the
297 ventral spinal cord (Fig. 3g). We further quantified the expression of these top lineage-
298 associated genes along the DV axis and found that *MSX1* was highly expressed in the dorsal
299 spinal cord, *FGFBP3* in central, and *OLIG2* in the mid-ventral domain from W5-8 (Fig. 3h,
300 Extended Data Fig. 8e). The spatial expression pattern of *MSX1* and *FGFBP3* disappeared at
301 W9, suggesting that the patterning of newborn ASCs and EPCs mainly took place before W8.
302 In contrast, *OLIG2* continued to show high ventral expression, while the mature OL-associated
303 gene *MBP* exhibited strong ventral expression at W12, which correlated with the appearance
304 of newborn mature OLs in the ventral spinal cord at W12 (Extended Data Fig. 3). These data
305 were validated by both ST (Extended Data Fig 8e) and HybISS (Extended Data Fig. 8c).

306 To further analyze the active TFs that regulate cell fate commitment, we performed regulon
307 analysis by SCENIC ¹⁷ in the scRNA-seq dataset. The analysis revealed the top regulons for
308 human spinal cord development as well as the gene expression of the top TFs (Extended Data
309 Fig. 9a-b), and we found that the top regulons were active in specific lineages during
310 neurogenesis and gliogenesis (Extended Data Fig. 9d). Most of the regulons for glial cells had
311 been active since W5 (Supplementary Figure 5a), indicating that NPCs were committed not
312 only to neuronal but also to glial fates at this early stage. This is also in line with gene
313 expression and validation by HybISS and IHC data above for early glial cells at W5 (Fig 2 a-
314 d, Extended Data Fig. 4h). Altogether, our analysis showed that the fate commitment of hNPCs
315 is spatiotemporally regulated by specific gene sets in the developing human spinal cord.

316

317 **The spatiotemporal genetic regulatory networks of human spinal cord development**

318 During neurodevelopment, hNPC differentiation follows a spatiotemporal pattern of cell fate
319 commitment, and is defined in specific progenitor and neuron domains along the DV axis ^{1,18}.
320 To better understand the regulatory controls (e.g., expression of TFs, morphogens, signaling
321 pathways, cell-cell interactions etc.), we first surveyed the most well-known signaling
322 pathways that have an impact on neural patterning, and found that the gene modules of WNT,
323 NOTCH and SHH signaling were expressed by most cell types (Fig. 4a) but overall decreased
324 overtime (Fig. 4b, Supplementary Figure 4). IHC showed that Active- β -Catenin (ABC) and
325 SHH pathway molecules (SHH, GLI1 and GLI3) at W5 were expressed in the roof plate and
326 floor plate respectively (Fig. 4c, Extended Data Fig 4e-f), but the expression decreased
327 dramatically after W8 (Fig. 4c). However, the NOTCH target HES1 showed overall high
328 expression level throughout the ventricle layer, without much DV biased expression (Extended
329 Data Fig 4g). Under the gradients of morphogens such as SHH and WNT, genes associated
330 with neurogenesis and gliogenesis (revealed by trajectory analysis) exhibited spatially specific

331 expression pattern at W5 and W8, which coincides with the spatial positions of their related
332 differentiated cell types, shown by HybISS (Fig. 4d). As variable genes used for analysis in the
333 scRNA-seq are dominated by differentiation during development, it was challenging to
334 spatially investigate and quantify the expression of neural patterning genes ^{7,19}. We used ST to
335 directly measure the expression of neural patterning genes, and created a detailed spatial gene
336 expression panel that indicates the DV patterning in the developing human spinal cord at early
337 stage (W5-8) (Fig 4e, Extended Data Fig. 10). Further, we quantified the expression of these
338 neural patterning genes, and showed that their spatially unique expression was also restricted
339 to certain developmental stages (i.e. progenitor patterning genes showing DV biased
340 expression at W5 and neuronal patterning at W5-8) (Fig. 4e).

341
342 Since multiple cells contribute to each spatial capture location in ST, we performed a co-
343 localization analysis using the proportion estimates obtained from *stereoscope*. This allowed
344 us to visualize the initiation of cell fate transition locally before migration starts. We found that
345 the ratio of NPCs decreased dramatically during development (Fig. 4f). At W5, the major
346 connections between NPCs to neurons and pre-glial cells represent initial differentiation. At
347 W8, the shared locations between INPs and different neurons suggested ongoing local
348 neurogenesis preceding neuronal migration. In contrast, the connections between NPCs and
349 glial cells were weak from W8, suggesting that soon after glial fate commitment migration of
350 the immature glial cells begins, during which further differentiation takes place (Fig. 4f). At
351 W12, the weak connections between NPCs and others, and strong connections among neurons
352 and glia suggested that the major events had shifted from differentiation to the formation of
353 neural circuits. In addition, TFs and cell-cell interaction analysis revealed other regulatory
354 networks such as top TFs in each cell type and cell-cell integrations via the most significant
355 ligand-receptor interactions (Supplementary Figure 4). This network analysis was in line with

356 our *in situ* data showing co-localization of NPC and neural cell markers at early developmental
357 stages (Fig. 3b and f, Extended Data Fig. 8c).

358

359 **Neurodevelopment involves species-specific events**

360 Most NPCs are believed to proliferate extensively before gliogenesis starts¹, we found that
361 more than half of the clusters expressed low levels of active cell cycle genes (S or G-to-M
362 phase) (Extended Data Fig. 6c). To address whether low proliferation is a specific phenotype
363 in humans, we integrated our scRNA-seq datasets with two mouse spinal cord development
364 datasets^{19,20} for normalized gene expression comparison (Fig 5a). In contrast to the majority of
365 hNPCs that had low expression of proliferation markers *MKI67* and *TOP2A* from W5-7, mouse
366 (m)NPCs were highly proliferative at least up to embryonic day (E) 13.5 (equivalent to human
367 W7) (Fig. 5b). One main mechanism that drives the quiescence of NPCs is the molecule *LRIG1*
368²¹, which showed much higher expression during embryonic and fetal stages of the human
369 spinal cord compared to mouse, in which high expression took place postnatally (Fig. 5b). In
370 agreement, IHC showed that many SOX9+ hNPCs were not expressing KI67 in the W5 human
371 spinal cord, differently from mouse E10.5 spinal cord containing mostly Sox9+Ki67+ cells,
372 confirming that most hNPCs in contrast to mNPCs entered quiescence during early
373 development (Fig. 5c).

374

375 Recent studies with scRNA-seq reveals that ASCs and OPCs are derived as early as gestational
376 week 8 (equivalent to post-conception week 6-7 in this study) in the developing human spinal
377 cord⁶. By using HybISS to validate lineage associated genes revealed by scRNA-seq, we found
378 these lineage-associated genes had been expressed in glial cells (*MSX1* in ASCs, *OLIG1* and
379 *OLIG2* in OPCs, and *FOXJ1* in EPCs) as early as W5, equivalent to E11 in mouse development.
380 It is known that the first mouse ASCs, OPCs and EPCs appear at E16.5, E12.5 and E15.5

381 respectively²²⁻²⁵, suggesting that hNPCs might have been committed to gliogenesis at earlier
382 stage of human neurodevelopment. Interestingly, *Msx1* has been shown to be the key regulator
383 for EPC differentiation during mouse spinal cord development²⁶, and we found that *MSX1* is
384 both a cell marker and a lineage-associated gene for human ASCs (Fig 1c, Fig 2a, Fig 3e-f).
385 By comparing gene expression in both ASCs and EPCs in the human-mouse integrated scRNA-
386 seq dataset, we found that *MSX1* was indeed highly expressed in *GFAP* expressing ASCs in
387 human spinal cord, but had low expression levels in mouse ASCs during development (Fig 5d).
388 In contrast, *MSX1* and *FOXJ1* were expressed in both mouse and human EPCs, suggesting that
389 *MSX1* has dual roles in regulating cell fate commitment of human ASC and EPC, but only
390 regulates EPCs in mice. We validated these results by performing ST at comparable timepoints
391 of human (W8) and mouse (E16) spinal cord sections. We found that the expression of *MSX1*
392 in humans was mainly located in the dorsal ventricular zone, and correlated with the marker
393 gene expression *GFAP* in ASCs and *FOXJ1* in EPCs (Fig 5e). However, in mouse sections,
394 *Msx1* was found to be expressed in the same area of *Foxj1*+ cells, but not in *Gfap*+ area, in line
395 with the previous study²⁶ showing *Msx1* is expressed in mouse ependymal cells during
396 development (Fig 5e).

397
398 To further compare the similarities and differences between mouse and human development,
399 we compared the most significant TF activities in human and mouse developing spinal cords
400 by regulon analysis (Extended Data Fig. 9 a and c). We found that some specific regulons
401 associated with certain human cell types (Extended Data Fig. 9a) also showed gene expression
402 in these cell types, but not in mice. For instance, *GLIS3* was highly associated with the fate
403 commitment of ASCs in human but little in mice, while *NKX6-1* was expressed in human
404 EPCs regulating their development but not expressed in mouse EPCs (Fig 5d). We further
405 confirmed these findings by ST, and showed that *GLIS3* was associated with *GFAP*+ area in

406 human but not mouse developing spinal cord (Fig 5e). Altogether, our data suggest that despite
407 the conserved mechanisms, there are fundamental differences of spatiotemporal gene
408 expression between mouse and human spinal cord development.

409

410 **Fetal human spinal cord and relation to ependymomas**

411 Ependymomas are highly aggressive CNS tumors with high recurrence rate ^{27,28}. Furthermore,
412 childhood ependymomas show much higher rates of anaplastic histology ²⁹, suggesting a larger
413 CSC population in the tumor. It has been suggested that the development of pediatric
414 ependymomas recapitulates neurodevelopment, but the previous studies on pediatric
415 ependymomas progression lacked proper normal human neurodevelopment datasets as
416 control^{27,28}. To demonstrate the potential of the human developmental atlas to reveal novel
417 biomarkers for disease diagnosis and potential treatment, we used our data to gain insight into
418 the molecular signature and differentiation of drug-resistant cancer stem cells (CSCs) in
419 pediatric ependymomas. We first obtained genes related to spinal cord tumor (HP:0010302)
420 from the Human Phenotype Ontology (HPO) database and plotted the module on ST data. We
421 observed broad but no regionally specific gene module expression of spinal cord tumor in all
422 ST sections (Fig. 6a), suggesting that many cell types in normal human developing spinal cord
423 are highly similar to spinal cord tumors. We integrated our scRNA-seq data with human
424 pediatric ependymomas ²⁸, unbiasedly transferred cell types from normal developmental data
425 to ependymomas, and showed that many cell types in normal tissue and in tumors were well
426 integrated (Fig. 6b, Supplementary Figure 6a). Despite the overlapping clusters of neural-cell-
427 like ependymoma with normal cells (Fig. 6c and f), most of the normal neuronal markers were
428 predominantly expressed in the normal neurons (Fig. 6d) while the normal glial markers were
429 similar between normal and tumor cells (Fig. 6g). The non-overlapping area probably suggests
430 that certain cell populations are unique to the respective condition (normal vs tumor). In the

431 field of cancer diagnosis and treatment, it is usually challenging to separate tumor and normal
432 cells to identify cancer-specific biomarkers. Therefore, we focused on comparing the
433 overlapping clusters between normal and tumor data, and identified tumor-specific genes such
434 as *CASC15* and microRNA *MIR99AHG* in neuron-like ependymomas, and *RPS14* and *RPS8*
435 in glia-like ependymomas (Fig. 6e, h). Moreover, many CSCs overlapped with normal NPCs
436 (Fig. 6g) and shared the expression of the classical NPC markers *SOX2* and *VIM* (Fig. 6j). After
437 identifying the putative CSC markers-associated clusters and proliferative clusters (cluster 3,
438 6, 7) (Supplementary Figure 6c, Fig 6j), we uncovered the CSC specific markers *FTX* and
439 *MIR99AHG*, which were not expressed in the normal hNPCs and thus could be novel
440 therapeutic targets for the ependymoma CSCs (Fig. 6i-k). We also plotted these CSC-specific
441 genes (e.g. *FTX* and *MIR99AHG*) in the ST dataset from normal human spinal cord sections as
442 independent validation, and did not find any expression in the sections (data not shown),
443 confirming that these genes are tumor-specific.

444

445 A previous study suggested that ependymoma-derived CSCs mimics neurodevelopment²⁸. To
446 further investigate the molecular differences between normal and cancer progenitors during
447 differentiation, our trajectory analysis showed that the EPC-related TFs *RFX2* and *RFX4* were
448 highly associated with two lineages of ependymal cell differentiation (Fig. 6l-m) and were
449 associated with both normal and tumor EPC differentiation. By screening the top lineage-
450 associated genes (Supplementary Figure 6b), we found that *NLRP1* and *VWA3B* were
451 specifically associated with normal ependymal and ependymal-like cancer cell differentiation,
452 respectively (Fig. 6n). Similarly, we found that *WLS* and *APOD* were highly associated with
453 the differentiation of ASCs (or ASC-like tumor) and OPCs (or OPC-like tumor) respectively
454 (Fig. 6 o-p). However, *FABP7* and *MSX1* were mainly associated with normal ASCs and
455 *OLIG2* and *OPCML* were mainly associated with normal OPCs and OLs (Fig.6 q-r,

456 Supplementary Figure 6b). In contrast, *FRMD5* and *GLUL* were mainly associated with ASCs-
457 like and OPCs/OLs-like ependymomas (Fig. 6 q-r, Supplementary Figure 6b) respectively.
458 Altogether, with our human spinal cord developmental atlas, we provide new insights of
459 normal human spinal cord development and potential diagnostic or therapeutic strategies in
460 human CNS tumors.

461

462 **An integrated atlas of spinal cord cell types across rodents and humans**

463 To compare cell type differences across species, timepoints, and technologies, we performed
464 stepwise data integration to integrate our human scRNA-seq data with publicly available
465 scRNA-seq datasets of spinal cord samples, including human development^{6,7}, mouse
466 embryonic development¹⁹, mouse postnatal development²⁰, mouse adulthood³⁰⁻³⁴ and datasets
467 suggested in a meta-analysis of mouse spinal cord atlases³⁵. We created an integrated cell atlas
468 with these 1.8 million cells (Fig 7a-c). We compared our cell type annotation results to the
469 original annotation from several datasets and found high correlations (Supplementary Figure
470 7). We then performed label transferred from our annotated cell types to the integrated dataset
471 (Fig 7a). Using the cell proportion from our dataset as a baseline for dataset comparison, we
472 found that our dataset (Li2022) shared high similarity with other comparable datasets of mouse
473 and human development, as shown in Zhang2021, Delile2019 and Rayon2021 (Fig 7d).
474 Notably, the Zhang2021 dataset includes some samples from second trimester of human spinal
475 cord development, but not much difference in OPCs and EPCs, suggesting a continuation of
476 glial cell differentiation but probably few newborn glial cell progenitors during the second
477 trimester in the developing human spinal cord. This large integrated dataset is now also
478 available together with the interactive map of our multi-omics data
479 (<https://tissuumaps.scilifelab.se/web/HDCA/SpinalCord2022/index.html>).

480

481

482 **Discussion**

483 In this study, by using multi-omics and data integration to study the developing human spinal
484 cord, we have: i) created a developmental cell atlas of the human spinal cord throughout the
485 first trimester of development, ii) revealed spatiotemporal regulation of human spinal cord
486 neurogenesis and gliogenesis, iii) presented major differences of cell and molecular regulation
487 between rodent and human spinal cord development, and iv) discovered unique markers and
488 regulation of CSC differentiation in human ependymomas.

489

490 The dynamics and molecular regulation of the human spinal cord development are still
491 understudied. While two recent studies explored the developing human spinal cord by scRNA-
492 seq and showed neural patterning and neurogenesis in identified clusters, they did not elucidate
493 how NPCs are committed to multiple neural cell lineages or how the spatiotemporal gene
494 expression is involved in neurogenesis and gliogenesis ^{6,7}. In this study, we acquired human
495 prenatal spinal cords over the first trimester for scRNA-seq and spatial techniques, integrated
496 the multi-omics datasets and validated the results, which gave new insights into the
497 spatiotemporal gene expression of the developing human spinal cord.

498

499 NPCs are believed to proliferate vividly during fetal development ¹. However, we found that
500 many hNPCs throughout the ventricular zone did not proliferate even at the early embryonic
501 stage. The proliferative NPCs lose their proliferation during the first trimester in humans, much
502 earlier than rodents. The loss of active NPCs after fetal development limits regeneration in the
503 mammalian adult spinal cord, for example after SCI ²⁴. The loss of active NPCs during first
504 trimester development in humans partly explains the extremely low regenerative potential in
505 human spinal cord. Interestingly, our results are in agreement with a previous study that the

506 stem cell quiescence-related gene *LRIG1*²¹ is one of the most significant gene in the non-
507 proliferative hNPCs, which could be targeted for reactivating hNPCs.

508

509 Since most lineage tracing techniques cannot be applied in humans, it is unclear how
510 neurogenesis and gliogenesis in human spinal cord are regulated in a spatiotemporal manner.
511 With integration of multi-omics data, we highlighted some unique developmental events in the
512 human developing spinal cord. First, by analyzing marker gene expression and active TFs,
513 validated by HybISS and IHC, we found that hNPCs were committed to glial fates as early as
514 W5 while previous studies on active regulons and marker expression showed that this occurred
515 at W8-10^{1,24,36}. Thus, our data pushes human gliogenesis to an earlier stage of
516 neurodevelopment. Second, while rodent astrocytes migrate horizontally during development
517 to the mantle zone and the future lateral white matter³⁶, we showed that human astrocytes were
518 first restricted in the dorsal region of the spinal cord. In addition, this process in humans was
519 spatiotemporally regulated by *MSX1*, a TF shown to specifically regulate ependymal cell
520 development in rodents²⁶. Third, we conclude that human EPCs exhibit a longer developmental
521 period than expected. Mouse spinal cord EPCs are derived from mid-late fetal stage (E15.5)
522 and are fully developed within one week *in vivo*²⁴. However, while we found that human EPCs
523 are derived from W5, a subpopulation that is located in the dorsal central canal of the human
524 adult spinal cord³⁷ was still missing at W12, suggesting a second wave of gliogenesis during
525 the second trimester. However, by comparing our data with data from Zhang et al., 2021⁶ that
526 includes second trimester samples, we did not observe a significant increase in the proportion
527 of EPCs (Fig. 7d). This could be due to a significant increase of other cell types during second
528 trimester, or technical issues of capturing EPCs during single cell collection from the second
529 trimester samples in other datasets. Future studies involving scRNA-seq and spatial techniques
530 is needed to fully describe gliogenesis in the human spinal cord. Importantly, by comparing

531 genetic regulation of human and mouse neurogenesis and gliogenesis, we found a number of
532 regulons and expressed genes that are only present in human spinal cord development and not
533 in mice, suggesting that neurodevelopment is regulated differently between species. Notably,
534 while most studies on neurogenesis and gliogenesis have focused only on the temporal gene
535 expression as molecular mechanisms, we developed a method to demonstrate that neural
536 patterning and positioning of neural cells are the results of the spatially biased expression in
537 addition to temporal gene expression.

538

539 Finally, we applied our developmental atlas of the human spinal cord to investigate gene
540 expression in childhood spinal ependymomas. Pediatric ependymomas are CNS tumors with
541 high recurrence rates, probably due to the proliferation of drug-resistant CSCs²⁸. In the field
542 of drug discovery and development, it is challenging to find cancer-specific markers to
543 selectively target cancer cells. We integrated our human spinal cord atlas with human pediatric
544 ependymomas data, and displayed the most significant differences of gene expression between
545 cancer and normal stem cells. Although CSCs and NPCs share similar lineage-associated genes
546 during differentiation, we could identify unique genes associated with normal NPC and CSC
547 differentiation respectively. Therefore, our results revealed molecular signatures of CSCs, and
548 their potential regulators at different stages during differentiation, which gives new insights
549 into specific targets for ependymoma treatments.

550

551 In conclusion, we provide a comprehensive analysis of the human first trimester spinal cord
552 during a critical phase of cellular specification and differentiation. While we confirm that
553 humans and rodents share multiple similar cellular and molecular mechanisms during
554 neurodevelopment, we discovered unexpected unique developmental events in the human
555 spinal cord. Our database will not only serve as developmental cell atlas resource, but also

556 provide important information for research on human neurodevelopmental disorders as well as
557 regenerative strategies and cancer treatments.

558

559 **Methods**

560 **Human prenatal tissue**

561 16 samples of human prenatal spinal cord tissue were used in the study (13 for scRNA-seq and
562 6 for ST, HybISS and IHC) representing post-conception weeks (W) 5, 6, 7, 8, 9, 10, 11, 12.
563 W5-8 is referred to as early stages (embryonic) while W9-12 is referred to as later first trimester
564 stages (fetal) in the present study. Post-conception age was determined by information from
565 the clinical ultrasound, time for last menstrual period, and by identifying age-dependent
566 anatomical landmarks with true crown-rump-length (CRL), taking into account that post-
567 conception age and clinical age differs by 1.5–2 weeks. The prenatal specimens were retrieved
568 from elective medical abortions at the Department of Gynecology, Danderyd Hospital and
569 Karolinska Huddinge Hospital after oral and written informed consent by the patient. All
570 patients were at least 18 years of age and Swedish-speaking. The clinical staff that informed
571 the patients and performed the abortions did not in any other way participate in this research.
572 The specimens were transported immediately from the clinic to the dissection laboratory. spinal
573 cord tissue was rapidly dissected in 4°C saline (Fresenius Kabi, B306443/01) under sterile
574 conditions within one-two hours after the abortion. Specific information can be found in
575 Supplementary Table 1. The use of prenatal tissue for this study was approved by the Swedish
576 Ethical Review Authority and the National Board of Health and Welfare. All procedures met
577 the ethical stipulations of the WMA Medical Ethics Manual and the Declaration of Helsinki,
578 and all experiments were performed in accordance with relevant guidelines and regulations.

579

580 **Preparation of human prenatal spinal cord for multi-omics**

581

582 ***scRNA-seq experiment***

583 The W5-W7 spinal cord tissues were used as one piece while W8-12 spinal cords were divided
584 into three pieces (cervical, thoracic, and lumbar regions) before dissociation. The dorsal root
585 ganglia were removed by cutting the roots. Each piece of tissue was minced into smaller pieces
586 using sterile blades and scissors. Artificial cerebrospinal (aCSF) was prepared as previously
587 described ¹⁶, with modification for Ca_2Cl_2 (1 mM) and MgCl_2 (2 mM). The aCSF was
588 oxygenated with 95% O_2 :5% CO_2 for 20 min at 4°C. The samples were then digested at 37°C
589 in aCSF. Papain solution (Worthington Biochemical; cat. no. LK003178; 20 U/ml in CSF) and
590 DNase I (Worthington Biochemical; cat. no. LK003172; 1mg/ml) were added to the aCSF to
591 dissociate the tissue. Incubation time was adjusted based on developmental stage, ranging from
592 15-25 minutes. The spinal cords were subsequently dissociated manually with fire-polished
593 glass pipettes. When most of the tissue was dissociated into single cells, the solution was
594 filtered using a 30 μm cell strainer (CellTrics, Sysmex, 04-0042-2316) and collected in a 15-ml
595 Falcon tube. The digestion solution was diluted with 7.5 ml of aCSF and centrifuged at 300g
596 for 5 min at 4°C. The pellets were resuspended in aCSF and transferred to Eppendorf tubes
597 pre-coated with 30% BSA (Sigma-Aldrich, 9048-46-8). After cell counting, the single cell
598 solution was diluted to a concentration of 800-1200 cells/ μl and kept on ice for immediate chip
599 loading.

600

601 ***ST and ISS experiments***

602 Human spinal cord tissues at W5, 8, 9 and 12 were embedded in Tissue-Tek (OCT) and snap-
603 frozen using an isopentane/dry ice slurry. W8-12 samples were first divided into cervical,
604 thoracic and lumbar. To enable spatial protein and gene expression analyses, the spinal cords
605 were cryosectioned at 16 μm thickness and alternately placed on Superfrost microscope glass

606 slides (Thermo Fisher Scientific) and Visium spatial gene expression slides (10x Genomics),
607 after which they were stored at -80°C for no more than XXX days before being used.

608

609 ***Immunohistochemistry***

610 Immunohistochemistry was performed as previously described ²⁴. Briefly, tissue sections were
611 rehydrated by 1X PBS for 5 min, then primary antibodies diluted in blocking solution (10%
612 normal donkey serum in PBS) were applied to the sections and incubated at room temperature
613 overnight. Secondary antibodies were applied to sections after 2 times wash with 1X PBS.
614 DAPI was applied on sections for 1 min. Sections were mounted after washing and ready for
615 confocal imaging by Zeiss LSM 700.

616

617 **Library preparation and sequencing**

618 ***scRNA-seq experiments***

619 Droplet-based single-cell RNA sequencing was performed using the 10x Genomics Chromium
620 Single Cell Kit v3. Single-cell suspensions concentrated at 800-1200 cells/ml were mixed with
621 master mix and nuclease-free water according to the Chromium manual, targeting 5000 cells
622 per reaction. The library preparation and sequencing were done according to the Chromium v3
623 standard protocol. Sequencing was performed using the Illumina NovaSeq 6000 with an
624 average 152,486 reads/cell.

625 ***ST experiments***

626 Spatial Gene Expression libraries were generated using Visium Spatial Gene Expression kit
627 from 10x Genomics (<https://support.10xgenomics.com/spatial-gene-expression>). Each Visium
628 barcoded glass slide contained 4 capture areas, each with ~5000 spots, and every spot contained
629 probes consisting of a spatial barcode, a unique molecular identifier (UMI) and a poly-dT-VN
630 sequence allowing for mRNA capture. The diameter of each spot was 55 μ m and the center-

631 to-center distance between the adjacent spots was 100 μ m. Several sections of the same post-
632 conceptional week were placed in each capture area, the number depending on the size of each
633 section. Sections were fixed for 30 min in methanol, stained with hematoxylin and eosin and
634 imaged using Metafer Slide Scanning system (Metasystem, Altlussheim, Germany). Optimal
635 permeabilization time for spinal cord sections was determined to be 20 min using 10x
636 Genomics Visium Tissue Optimization Kit. In total, Visium Spatial Gene Expression libraries
637 from 76 spinal cord sections were prepared by following the manufacturer's protocol. Libraries
638 were sequenced using Illumina platform (NovaSeq6000, NextSeq2000). The number of cycles
639 for read 1 was 28 bp and 120 bp for read 2.

640 ***HybISS***

641 HybISS was performed as reported by Gyllborg et al.⁵. Briefly, after fixation, sections were
642 permeabilized with 0.1 M HCl and washed with PBS. SecureSeal™ Hybridization Chambers
643 (Grace Bio-Labs) were applied around tissue sections and cDNA synthesized by reverse
644 transcribing overnight with reverse transcriptase (BLIRT), RNase inhibitor, and priming with
645 random decamers. The next day, sections were post-fixed before PLP hybridization and
646 ligation at a final concentration of 10 nM/PLP, with Tth Ligase and RNaseH (BLIRT). This
647 was performed at 37°C for 30 min and then moved to 45°C for 1.5 h. Sections were washed
648 with PBS and RCA was performed with phi29 polymerase (Monserate) and Exonuclease I
649 (Thermo Scientific) overnight at 30°C. SecureSeal chambers were then removed. Bridge-
650 probes (10 nM) were hybridized at RT for 1 h in hybridization buffer (2XSSC, 20%
651 formamide). This was followed by hybridization of readout detection probes (100 nM) and
652 DAPI (Biotium) in hybridization buffer for 1 h at RT. Sections were washed with PBS and
653 mounted with SlowFade Gold Antifade Mountant (Thermo Fisher Scientific). After each
654 imaging round, coverslips were removed and sections washed 5 times with 2XSSC and then
655 bridge-probe/detection oligos were stripped with 65% formamide and 2XSSC for 30 min at

656 30°C. This was followed by 5 washes with 2XSSC. Then the process was repeated for the next
657 cycle of bridge-probes hybridization.

658 For subtype / cell state markers, Kits from 10x Genomics were provided along with an
659 accompanying protocol (High Sensitivity kit). In summary, the tissue was fixed, and then the
660 direct RNA probe mixture was added (incubated overnight at 37°C). The section was
661 subsequently washed and ligation mix was added (incubated at 37 °C for 2 h). Following
662 washing, rolling circle amplification was performed at 30°C overnight. Lastly, rounds of
663 labeling and stripping were done for detection.

664 Imaging was performed with a Leica DMI8 epifluorescence microscope equipped with an LED
665 light source (Lumencor® SPECTRA X), sCMOS camera (Leica DFC9000GTC), and 20×
666 objective (HC PL APO, 0.80). Each field-of-view (FOV) was imaged with 24 z-stack planes
667 with 0.5 μm spacing and 10% overlap between FOVs.

668

669 **Sequence alignment and annotation**

670 ***scRNA-seq experiments***

671 Single-cell sequencing data were processed using the CellRanger pipeline (version 3.0.2; 10x
672 Genomics). Reads were mapped against the human genome (ENSEMBL genome assembly,
673 release 93) and annotated with GENCODE gene annotations for the GRCh38-3.0.0 genome
674 assembly (GENCODE release 32). Using the BAM files from CellRanger, molecules were
675 mapped into spliced and unspliced transcripts using velocyto (0.17.17) into which loom files
676 were generated for each sample.

677 ***ST experiments***

678 Sequenced Spatial Transcriptomics libraries were processed using the Space Ranger v1.0.0
679 pipeline(10X Genomics). Reads were aligned to the human reference genome (ENSEMBL

680 genome assembly, release 93) and annotated using GRCh38-3.0.0 to obtain expression
681 matrixes.

682

683 **Data quality and filtering**

684 *scRNA-seq experiments*

685 The single-cell count matrix was first enriched for protein-coding RNA and lincRNA gene
686 types. Cells with fewer than 500 genes, and genes expressed in fewer than 15 cells were
687 excluded from the analysis. Cells with over 25% mitochondrial gene expression were also
688 excluded.

689 *ST experiments*

690 In total, 76 tissue sections were analyzed, resulting in 20835 spots used for data analysis. The
691 count matrix was enriched for protein-coding and lincRNA genes. Count matrix was filtered
692 for all hemoglobin related genes, *MALAT1*, mitochondrial and ribosomal protein coding genes.
693 Spots with fewer than 500 genes and genes expressed in fewer than 5 spots were excluded from
694 analysis of the three post-conception time points.

695

696 **Data analysis**

697 *Analysis for scRNA-seq and ST data*

698 Normalization, dimensionality reduction, and clustering of scRNA-seq data were performed
699 using the Seurat package (Seurat v4.0.1)³⁸, and the top 6000 genes with high dispersion were
700 selected using the FindVariableGenes function. Cell cycle activity, number of genes, and
701 mitochondrial content across the data were regressed out using the ScaleData function.
702 Principal component analysis (PCA) was performed on the 50 most significant components as
703 determined by the PCElbowPlot function, showing the standard deviation of the principal
704 components. Cells in different cycling stages were identified by gene sets called “S.Score”,

705 “G2M.Score” within the Seurat package. Clusters were identified using the FindClusters
706 function by using Louvain resolution 1.2 for scRNA-seq.

707

708

709 Analysis, including data normalization, dimensionality reduction and clustering, of ST data
710 were performed jointly using the Seurat and STUtility packages. Normalization was conducted
711 using variance stabilizing transformation (SCTransform). Principal Component Analysis
712 (PCA) was used for selection of significant components, a total of 50 principal components
713 were used in downstream analysis and 30 principal components for ST analysis. To integrate
714 ST sections Harmony (RunHarmony, version 1.0) function was used. Spots were clustered
715 using the Shared Nearest Neighbor algorithm implemented in the Seurat package as
716 FindNeighbors and FindClusters (Louvain resolution 0.7).

717

718 Uniform Manifold Approximation and Projection (UMAP) was used to create a 2D embedding
719 of cell or spot transcription profiles for visualization purposes (RunUMAP). Identification of
720 differentially expressed genes among clusters was done using the FindAllMarkers function
721 from the Seurat package, where genes with log fold changes above 0.2 and p-values below 0.01
722 were considered significant. For the scRNA-seq data, a sub-selection of 50 random cells per
723 cluster were used in order to compensate for differences in cell composition bias per cluster.
724 For integration of scRNA-seq data and ST data we used stereoscope ¹¹, which performs guided
725 decomposition of the mixed expression data collected from each spatial capture location, using
726 profiles learnt from scRNA-seq data as a reference. In the stereoscope analysis, a batch size of
727 2048 and 50000 epochs was used for both the parameter estimation step and the proportion
728 inference process. Cell types with fewer than 25 cells were excluded from the analysis, while
729 we randomly selected 500 cells from cell types with more than 500 members. For cell types

730 with more than 25 members and less than 500 members, all cells were included. In the analysis,
731 2000 highly variable genes were used. These genes were extracted by applying the function
732 `scanpy.pp.highly_variable_genes()` with `n_top_genes=2000` from the `scanpy`
733 (`v.1.8.0.dev78+gc488909a`) suite, after having normalized
734 (`scanpy.pp.normalize_total(...,target_sum=1e4)`) and log-transformed (`scanpy.pp.log1p(...)`)
735 the data. Cell type decomposition of ST spots was then saved as an assay for downstream
736 analysis.

737

738 GO characteristics of gene clusters were determined using the `clusterProfiler` package (version
739 3.8.1)³⁹ for all DE genes with an average logFC value above zero, and an adjusted p-value
740 below 0.01. The `compareCluster` function was used with a `pvalueCutoff = 0.05`. Analysis of
741 genes belonging to Wnt, Shh or Notch pathways as well as Human Spinal Cord development
742 were done using the KEGG database and Phenotype Orthologs (HPO), respectively.

743

744 For previously published scRNAseq data used in this study, data sources are listed below under
745 the section Data availability. All these datasets were processed the same way as their
746 publication stated.

747

748 ***Cell type annotation***

749 After pre-processing and clustering analysis, each cluster (for both scRNA-seq and ST) was
750 manually annotated based on previous knowledge and recent atlas resources. After annotating
751 each cluster, clusters with the same major cell type names were merged and DEG analysis on
752 these major cell types were performed in an unsupervised manner. These DEG results
753 confirmed the accuracy of annotation. In addition, all available spinal cord scRNA-seq datasets

754 (by June 2022) were integrated, and correlation analysis for annotations was performed, which
755 showed high correlation between our dataset annotation and previous studies.

756

757 ***Inference of branching trajectories***

758 The R package slingshot (version 1.8.0) ¹⁵ was used to analyze neurogenesis and gliogenesis
759 respectively. For neurogenesis, the NPC cluster close to intermediate neuronal progenitors
760 (INPs), all the INPs and all differentiated neurons were selected. For gliogenesis, we selected
761 all glial cells and all NPCs that were connected to the trajectory. For each branch, clusters in
762 the upstream and downstream were selected for pseudotime analysis. Lineage-associated genes
763 were calculated by the R package TradeSeq (version 1.4.0) ⁴⁰.

764

765 The R package URD (version 1.1.1) ¹⁴ was used to build differentiation trajectories during
766 development. In the neurogenesis and gliogenesis analysis, a population of cells that were
767 sampled from W5, clustered as NPCs_10, and with higher expression of *TOP2A* and *SOX2*
768 was identified and used as root in the URD trajectory reconstruction. The tips of ASCs, OLs,
769 EPCs, ExNs, ChNs and 3 IbNs lineages were identified based on the Louvain clusters (with a
770 resolution 1.2), separately. After 350,000 simulated random walks were performed per tip, the
771 divergence method “preference” was used to build the tree, with minimum.visits = 2,
772 cells.per.pseudotime.bin = 25, bins.per.pseudotime.window = 8, p.thresh = 0.05 and
773 min.cells.per.segment = 10.

774

775 In the inference of hNPC development trajectory, same population of NPCs was used as root,
776 and the NPCs with later pseudotime estimated by scVelo and closer to neuronal and glial
777 lineages on UMAP were identified as tips, respectively. The divergence method “preference”

778 was also used for tree building, with cells.per.pseudotime.bin = 25,
779 bins.per.pseudotime.window = 8, p.thresh = 0.001 and other parameters default.

780

781 ***Estimation of RNA velocities***

782 The transcriptional dynamics of splicing kinetics were modelled stochastically with scVelo
783 (version 0.2.4)¹³ and projected onto the UMAP embedding as streamlines. To show the
784 connectivity between different clusters, the transition probabilities of cell-to-cell transitions
785 were estimated and projected onto the same UMAP embedding.

786

787 ***Inference of transcription factor activity***

788 The SCENIC software (version 0.11.2)¹⁷ was used to infer TF activities in human and mouse
789 neural cells separately. In the human dataset, 10% cells in each subtype were randomly sampled
790 and combined to infer gene regulatory network with GRNBoost2 algorithm. Then all neural
791 cells were used to predict candidate regulons (cisTarget) and to estimate the cellular enrichment
792 of the predicted regulons (AUCell). The top 5 regulons with the highest specificity in each cell
793 type were selected using the regulon_specificity_scores() function implemented in Python. For
794 each regulon, its activity in all cells was fitted and binarized to determine the “on” or “off”
795 state, and further used to compute the “percent activated” in the Dot plots (Extended Data Fig.
796 10 and Supplementary Figure5).

797

798 The glial cells and neuronal cells were separately subset and the subtype specificity was
799 recalculated within the subsets. Same analysis pipeline was applied to the mouse dataset,
800 except that all mouse neural cells were used in the network inference step (instead of 10%
801 random sampling).

802

803 ***Calculation of dorsal-ventral axis gene expression***

804 In order to assess how certain feature values (e.g., gene expression or cell type proportions)
805 varies along the dorsal-ventral (DV) axis, we designed a method to cast the 2D data into a
806 different and more informative 1D representation relating to the aforementioned axis. More
807 specifically, we sought to model the feature value as a function of the position along the DV-
808 axis, that is $y_i = f(x_i)$, where y_i is the feature value of observation i while x_i is the position of
809 said observation on the DV-axis. Below we describe in detail how we obtained the values y_i
810 and x_i as well as the character of the non-parametric function f .

811

812 First, to determine each observation's position along the DV-axis, we had to define the DV-
813 axis in each sample. Thus, we manually annotated all observations (spots) as either belonging
814 to the ventral or dorsal region. We denoted the (mutually exclusive) sets of spots in the dorsal
815 and ventral regions as D respectively V , we also let $|\cdot|$ represent the cardinality operator. Then,
816 we selected a subset of observations (D' and V') of size $\min(|D|, 200)$ respectively $\min(|V|, 100)$
817 from each set, and computed the “DV-difference vectors” δ_s according to:

$$818 \quad \delta_s = v_k - d_s, \quad v_k = \operatorname{argmin}_{v_k} \|d_s - v_k\|, \quad v_k \in V', \quad d_s \in D'$$

819 Whereafter we calculated the “average DV-difference vector”, representing the direction of
820 the DV-axis, as follows:

$$821 \quad \bar{\delta}_s = \frac{1}{|D'|} \sum_s \delta_s$$

822 Finally, we let the axis vector a be defined as the normalized (to unit norm) average, across
823 all observations within the sample, DV-difference vector. We then proceeded to project each
824 observation's spatial coordinates (in 2D space) onto the (1D) axis vector a , as to obtain its
825 position along the DV-axis (ps); for this, standard orthogonal projection is used:

826
$$p_s = \text{proj}_a u_s = \frac{u_s \cdot a}{a \cdot a} a = (u_s \cdot a) \cdot a$$

827 Where u_s is an observation's original coordinates in the 2D plane, the final equality holds
828 true since a has unit norm. For each sample, we then normalized the axis projections using
829 min-max scaling (subtraction of minimal value and division with the difference between
830 maximal and minimal values). For computational reasons, we assign each observation s
831 (based on their axis projection value) to one bin (b_i) of $nbins$ different bins, according to:

832
$$p_s \geq (i - 1) \cdot (nbins)^{-1} \wedge p_s < i \cdot (nbins)^{-1} \rightarrow s \in b_i \quad \forall i \in \{0, 1, \dots, nbins\}$$

833 Next, for each bin b_i we compute the average axis value (x_i) and average feature value (y_i) as
834 follows:

835
$$x_i = \frac{1}{|b_i|} \sum_{s \in b_i} p_s, \quad y_i = \frac{1}{|b_i|} \sum_{s \in b_i} v_s$$

836 Where v_s is the feature value associated with observation s . In the last step, we aim to relate
837 the feature values to the axis positions via a function f . The character of f is determined by
838 loess regression (locally estimated scatterplot smoothing), implemented with
839 `geom_smooth(..., method = loess)` from the R package `ggplot2` and visualized as a 1D plot -
840 generating the plots similar to those shown (for example) in Figure 3h.

841

842 We implemented this method in R, and all code is available at GitHub
843 (<https://github.com/almaan/axis-projection>) as a package that can be installed and used in a
844 standard R environment.

845

846 ***Image processing and decoding for HybISS data***

847 After imaging, Leica LAS X software was used to maximum intensity project each field of
848 view (FOV) to obtain a flattened two-dimensional image. Imaging data was then analyzed with
849 in-house custom software that handles image processing and gene calling based on the python

850 package Starfish. Each two-dimensional FOV was exported, and preprocessed by alignment
851 between cycles, and stitched together using the MIST algorithm ⁴¹. Stitching was followed by
852 retiling to create smaller non-overlapping 2000x2000 pixel images that were then used for
853 decoding. The decoding pipeline can be found on the Moldia GitHub page
854 (https://github.com/Moldia/iss_starfish/). In short, the images were initially registered (using
855 the LearnTransform module in Starfish) and filtered (using the Filter module from Starfish)
856 using a white top hat filter with a masking radius of 15. The filtered images are subsequently
857 normalized (using the Filter module from Starfish). Following the normalization, spots were
858 detected using the FindSpots module from Starfish and subsequently decoded using
859 MetricDistance decoding.

860 ***Probabilistic cell typing for HybISS data***

861 Probabilistic cell maps were created using probabilistic cell typing by in situ sequencing
862 (pciSeq). The pciSeq pipeline can be found at <https://github.com/acycliq/pciSeq> and is
863 described in Qian et al. ¹² In short, pciSeq works by assigning genes to cells and then cells to
864 cell types, and this assignment is done using a probabilistic framework based on a single-cell
865 RNA sequencing data ¹². Due to the density of nuclei in the tissue, nuclear segmentation could
866 not be done, instead a compartment-based approach was employed in which each compartment
867 was defined as 40x40 pixel grid (roughly 13x13 μm).

868

869 **Quantification and Statistical Analysis**

870 Significance of scRNA-seq and ST analysis for differential gene expression were carried out
871 using Wilcox. Genes with $P < 0.001$ were selected as significantly different expressed genes.
872 Significantly different expressed gene lists were ordered and filtered by smallest P value the
873 biggest changes of log Fc.

874

875 **Data and Code Availability**

876 Codes for analysis of this paper can be found from the link:

877 https://github.com/czarnewski/human_developing_spinal_cord

878 Data will be made publicly available on Gene Expression Omnibus (GEO) upon publication.

879 The publicly available data utilized in this study are available at:

880 Sathyamurthy: <https://www.ncbi.nlm.nih.gov/geo/query/acc.cgi?acc=GSE103892>

881 Zeisel: <https://www.ncbi.nlm.nih.gov/sra/SRP135960>

882 Rosenberg: <https://www.ncbi.nlm.nih.gov/geo/query/acc.cgi?acc=GSE110823>

883 Blum: <https://www.ncbi.nlm.nih.gov/geo/query/acc.cgi?acc=GSE161621>

884 Alkaslasi: <https://www.ncbi.nlm.nih.gov/geo/query/acc.cgi?acc=GSE167597>

885 Delile: <https://www.ebi.ac.uk/arrayexpress/experiments/E-MTAB-7320/files>

886 Rayon: <https://www.ncbi.nlm.nih.gov/geo/query/acc.cgi?acc=GSE171892>

887 Milich: <https://www.ncbi.nlm.nih.gov/geo/query/acc.cgi?acc=GSE162610>

888 Zhang: <https://www.ncbi.nlm.nih.gov/geo/query/acc.cgi?acc=GSE136719>

889 Gojo (ependymomas): <https://www.ncbi.nlm.nih.gov/geo/query/acc.cgi?acc=GSE141460>

890

891 **References**

- 892 1 Guérout, N., Li, X. & Barnabé-Heider, F. Cell fate control in the developing central
893 nervous system. *Exp Cell Res* **321**, 77-83 (2014).
<https://doi.org/10.1016/j.yexcr.2013.10.003>
- 894 2 Curtis, E. *et al.* A First-in-Human, Phase I Study of Neural Stem Cell Transplantation
895 for Chronic Spinal Cord Injury. *Cell Stem Cell* **22**, 941-950 e946 (2018).
<https://doi.org/10.1016/j.stem.2018.05.014>
- 896 3 Xu, N. *et al.* Transplantation of Human Neural Precursor Cells Reverses Syrinx Growth
897 in a Rat Model of Post-Traumatic Syringomyelia. *Neurotherapeutics* (2021).
<https://doi.org/10.1007/s13311-020-00987-3>
- 898 4 Asp, M. *et al.* A Spatiotemporal Organ-Wide Gene Expression and Cell Atlas of the
899 Developing Human Heart. *Cell* **179**, 1647-1660.e1619 (2019).
<https://doi.org/10.1016/j.cell.2019.11.025>
- 900 5 Gyllborg, D. *et al.* Hybridization-based *in situ* sequencing (HybISS) for spatially
901 resolved transcriptomics in human and mouse brain tissue. *Nucleic Acids Res* **48**, e112
902 (2020). <https://doi.org/10.1093/nar/gkaa792>

907 6 Zhang, Q. *et al.* Single-cell analysis reveals dynamic changes of neural cells in
908 developing human spinal cord. *EMBO Rep* **22**, e52728 (2021).
909 <https://doi.org/10.15252/embr.202152728>

910 7 Rayon, T., Maizels, R. J., Barrington, C. & Briscoe, J. Single-cell transcriptome
911 profiling of the human developing spinal cord reveals a conserved genetic programme
912 with human-specific features. *Development* **148** (2021).
913 <https://doi.org/10.1242/dev.199711>

914 8 Marklund, U. *et al.* Detailed expression analysis of regulatory genes in the early
915 developing human neural tube. *Stem Cells Dev* **23**, 5-15 (2014).
916 <https://doi.org/10.1089/scd.2013.0309>

917 9 Bayer, S. A. & Altman, J. in *Atlas of human central nervous system development* 522
918 p.

919 10 Bayer, S. A. & Altman, J. in *Atlas of human central nervous system development* ; v. 4
920 577 p.

921 11 Andersson, A. *et al.* Single-cell and spatial transcriptomics enables probabilistic
922 inference of cell type topography. *Commun Biol* **3**, 565 (2020).
923 <https://doi.org/10.1038/s42003-020-01247-y>

924 12 Qian, X. *et al.* Probabilistic cell typing enables fine mapping of closely related cell
925 types *in situ*. *Nat Methods* (2019). <https://doi.org/10.1038/s41592-019-0631-4>

926 13 Bergen, V., Lange, M., Peidli, S., Wolf, F. A. & Theis, F. J. Generalizing RNA velocity
927 to transient cell states through dynamical modeling. *Nat Biotechnol* **38**, 1408-1414
928 (2020). <https://doi.org/10.1038/s41587-020-0591-3>

929 14 Farrell, J. A. *et al.* Single-cell reconstruction of developmental trajectories during
930 zebrafish embryogenesis. *Science* **360** (2018). <https://doi.org/10.1126/science.aar3131>

931 15 Street, K. *et al.* Slingshot: cell lineage and pseudotime inference for single-cell
932 transcriptomics. *BMC Genomics* **19**, 477 (2018). <https://doi.org/10.1186/s12864-018-4772-0>

934 16 La Manno, G. *et al.* RNA velocity of single cells. *Nature* **560**, 494-498 (2018).
935 <https://doi.org/10.1038/s41586-018-0414-6>

936 17 Aibar, S. *et al.* SCENIC: single-cell regulatory network inference and clustering. *Nat
937 Methods* **14**, 1083-1086 (2017). <https://doi.org/10.1038/nmeth.4463>

938 18 Lu, D. C., Niu, T. & Alaynick, W. A. Molecular and cellular development of spinal
939 cord locomotor circuitry. *Front Mol Neurosci* **8**, 25 (2015).
940 <https://doi.org/10.3389/fnmol.2015.00025>

941 19 Delile, J. *et al.* Single cell transcriptomics reveals spatial and temporal dynamics of
942 gene expression in the developing mouse spinal cord. *Development* **146** (2019).
943 <https://doi.org/10.1242/dev.173807>

944 20 Rosenberg, A. B. *et al.* Single-cell profiling of the developing mouse brain and spinal
945 cord with split-pool barcoding. *Science* **360**, 176-182 (2018).
946 <https://doi.org/10.1126/science.aam8999>

947 21 Marqués-Torrejón, M. *et al.* LRIG1 is a gatekeeper to exit from quiescence in adult
948 neural stem cells. *Nat Commun* **12**, 2594 (2021). <https://doi.org/10.1038/s41467-021-22813-w>

950 22 Barry, D. & McDermott, K. Differentiation of radial glia from radial precursor cells
951 and transformation into astrocytes in the developing rat spinal cord. *Glia* **50**, 187-197
952 (2005). <https://doi.org/10.1002/glia.20166>

953 23 Marques, S. *et al.* Transcriptional Convergence of Oligodendrocyte Lineage
954 Progenitors during Development. *Dev Cell* **46**, 504-517.e507 (2018).
955 <https://doi.org/10.1016/j.devcel.2018.07.005>

956 24 Li, X. *et al.* Regenerative Potential of Ependymal Cells for Spinal Cord Injuries Over
957 Time. *EBioMedicine* **13**, 55-65 (2016). <https://doi.org/10.1016/j.ebiom.2016.10.035>

958 25 Li, X. *et al.* FoxJ1 regulates spinal cord development and is required for the
959 maintenance of spinal cord stem cell potential. *Exp Cell Res* **368**, 84-100 (2018).
960 <https://doi.org/10.1016/j.yexcr.2018.04.017>

961 26 Ghazale, H. *et al.* RNA Profiling of the Human and Mouse Spinal Cord Stem Cell
962 Niches Reveals an Embryonic-like Regionalization with MSX1. *Stem Cell Reports* **12**,
963 1159-1177 (2019). <https://doi.org/10.1016/j.stemcr.2019.04.001>

964 27 Byer, L. *et al.* A systematic review and meta-analysis of outcomes in pediatric,
965 recurrent ependymoma. *J Neurooncol* **144**, 445-452 (2019).
966 <https://doi.org/10.1007/s11060-019-03255-3>

967 28 Gojo, J. *et al.* Single-Cell RNA-Seq Reveals Cellular Hierarchies and Impaired
968 Developmental Trajectories in Pediatric Ependymoma. *Cancer Cell* **38**, 44-59 e49
969 (2020). <https://doi.org/10.1016/j.ccel.2020.06.004>

970 29 Elsamadicy, A. A. *et al.* Comparison of epidemiology, treatments, and outcomes in
971 pediatric versus adult ependymoma. *Neurooncol Adv* **2**, vdaa019 (2020).
972 <https://doi.org/10.1093/noajnl/vdaa019>

973 30 Milich, L. M. *et al.* Single-cell analysis of the cellular heterogeneity and interactions in
974 the injured mouse spinal cord. *J Exp Med* **218** (2021).
975 <https://doi.org/10.1084/jem.20210040>

976 31 Blum, J. A. *et al.* Single-cell transcriptomic analysis of the adult mouse spinal cord
977 reveals molecular diversity of autonomic and skeletal motor neurons. *Nat Neurosci* **24**,
978 572-583 (2021). <https://doi.org/10.1038/s41593-020-00795-0>

979 32 Zeisel, A. *et al.* Molecular Architecture of the Mouse Nervous System. *Cell* **174**, 999-
980 1014 e1022 (2018). <https://doi.org/10.1016/j.cell.2018.06.021>

981 33 Sathyamurthy, A. *et al.* Massively Parallel Single Nucleus Transcriptional Profiling
982 Defines Spinal Cord Neurons and Their Activity during Behavior. *Cell Rep* **22**, 2216-
983 2225 (2018). <https://doi.org/10.1016/j.celrep.2018.02.003>

984 34 Alkaslasi, M. R. *et al.* Single nucleus RNA-sequencing defines unexpected diversity of
985 cholinergic neuron types in the adult mouse spinal cord. *Nat Commun* **12**, 2471 (2021).
986 <https://doi.org/10.1038/s41467-021-22691-2>

987 35 Russ, D. E. *et al.* A harmonized atlas of mouse spinal cord cell types and their spatial
988 organization. *Nat Commun* **12**, 5722 (2021). [https://doi.org/10.1038/s41467-021-25125-1](https://doi.org/10.1038/s41467-021-
989 25125-1)

990 36 Hochstim, C., Deneen, B., Lukaszewicz, A., Zhou, Q. & Anderson, D. J. Identification
991 of positionally distinct astrocyte subtypes whose identities are specified by a
992 homeodomain code. *Cell* **133**, 510-522 (2008).
993 <https://doi.org/10.1016/j.cell.2008.02.046>

994 37 Ghazale, H. *et al.* RNA Profiling of the Human and Mouse Spinal Cord Stem Cell
995 Niches Reveals an Embryonic-like Regionalization with MSX1(+) Roof-Plate-Derived
996 Cells. *Stem Cell Reports* **12**, 1159-1177 (2019).
997 <https://doi.org/10.1016/j.stemcr.2019.04.001>

998 38 Hao, Y. *et al.* Integrated analysis of multimodal single-cell data. *Cell* **184**, 3573-
999 3587.e3529 (2021). <https://doi.org/10.1016/j.cell.2021.04.048>

1000 39 Yu, G., Wang, L. G., Han, Y. & He, Q. Y. clusterProfiler: an R package for comparing
1001 biological themes among gene clusters. *OMICS* **16**, 284-287 (2012).
1002 <https://doi.org/10.1089/omi.2011.0118>

1003 40 Van den Berge, K. *et al.* Trajectory-based differential expression analysis for single-
1004 cell sequencing data. *Nat Commun* **11**, 1201 (2020). [https://doi.org/10.1038/s41467-020-14766-3](https://doi.org/10.1038/s41467-
1005 020-14766-3)

1006 41 Chalfoun, J. *et al.* MIST: Accurate and Scalable Microscopy Image Stitching Tool with
1007 Stage Modeling and Error Minimization. *Sci Rep* 7, 4988 (2017).
1008 <https://doi.org/10.1038/s41598-017-04567-y>
1009

1010 **Acknowledgements**

1011 The study was supported by the Erling Persson Family Foundation, Knut and Alice Wallenberg
1012 Foundation and the research funds of Karolinska Institutet and Science for Life Laboratory.
1013 P.C. is partly financially supported by the Knut and Alice Wallenberg Foundation as part of
1014 the National Bioinformatics Infrastructure Sweden at SciLifeLab. The National Genomics
1015 Infrastructure (NGI), Sweden is acknowledged for providing infrastructure support. Chan
1016 Zuckerberg Initiative, an advised fund of Silicon Valley Community Foundation [2018-
1017 191929] and the Swedish Research Council [2019-01238] to M.N.; Swedish Brain Foundation
1018 (Hjärnfonden) [PS2018-0012] to D.G; Chinese Scholarship Council to Y.L.

1019 The authors acknowledge the support by the Karolinska Institutet Developmental Tissue Bank
1020 for providing human fetal tissues.

1021

1022 **Author information:** X.L. designed the study, planned, and performed the experiments
1023 (human tissue dissection, scRNA-seq, ST and HybISS), analyzed the scRNA-seq data,
1024 interpreted bioinformatic results (scRNA-seq, ST, HybISS and IHC) and biological results,
1025 wrote the manuscript, and designed and prepared figures. Za.A. performed ST experiments,
1026 analyzed the ST data, interpreted results, and designed figures. P.C. guided bioinformatic data
1027 analysis, interpreted results and designed figures. A.A. conducted the stereoscope analysis and
1028 developed the method to examine feature values along the DV-axis. C.M.L. analyzed the
1029 HybISS data and prepared figures. Y.L. participated in trajectory analysis. D.G. performed
1030 HybISS experiments and guided HybISS data analysis. E.B. performed scRNA-seq
1031 experiments. L.L. guided data analysis for ST. L.H. supported scRNA-seq experiments. Zh.A.
1032 performed IHC. H.K.K. managed the collection of prenatal human tissue. E.Å. dissected and

1033 staged the tissue material. M.N. guided HybISS experiments. S.L. guided scRNA-seq
1034 experiments. I.A. participated in experimental and data analysis discussion. J.L. guided ST
1035 experiments. E.S. conceived and designed the study, dissected, and staged the tissue materials,
1036 provided biological guidance, supported biological result interpretation, and wrote the
1037 manuscript. All authors helped with manuscript preparation.

1038

1039 **Ethics declarations:**

1040 Z.A., L.L., J.L. are consultants, and M.N. advisor for 10x Genomics Inc.

1041

1042

1043

1044

1045

1046

1047

1048

1049

1050

1051

1052

1053

1054

1055

1056

1057

1058

1059

1060

1061

1062

1063

1064

1065

1066

1067

1068

1069

1070

1071

1072

1073

1074

1075 **Figure Legends:**

1076 **Fig. 1: Comprehensive atlas of the developing human spinal cord.** a) Schematic overview
1077 of the workflow. b) UMAP of scRNA-seq datasets revealing major cell populations. c) Dot
1078 plot illustrating top marker genes for major cell populations. d) Spatial mapping of major cell
1079 types from ST analysis in representative human spinal cord sections. e) Representative
1080 stereoscope plots of one W12 section. f) Representative images and cell typing results from
1081 HybISS. Scale bar = 200 μ m. Neural stem and progenitor cells (NPCs), intermediate neuronal
1082 progenitors (INPs), excitatory neurons (ExNs), inhibitory neurons (IbNs), cholinergic neurons
1083 (ChNs), astrocytes (ASCs), ependymal cells (EPCs), oligodendrocyte precursor cells (OPCs),
1084 oligodendrocytes (OLs), immune cells (Immune), Schwann cells (SWCs), pericytes (PCs),
1085 endothelial cells (ENs) and vascular capillary endothelial cells (VCLPs).

1086
1087 **Fig. 2: Heterogenous neural cells in the human developing spinal cord.** a) Representative
1088 images showing validation of newborn neurons and glial cells in the developing human spinal
1089 cord by HybISS. Scale bar 200 μ m. b) Representative confocal images showing
1090 immunostaining of newborn astrocytes (b) and ependymal cells (c) at W5, while OPCs are not
1091 born at W5 yet (d). Scale bar =200 μ m and 50 μ m for low and high magnification respectively.
1092 Rectangles indicate enlarged areas. e) UMAP illustrating the heterogenous cell types or cell
1093 states of different neural cell populations.

1094
1095 **Fig. 3: Spatiotemporal regulation of human neurogenesis and gliogenesis.** a) UMAP
1096 displaying branches from NPCs to different neuronal clusters, confirmed by RNA velocity (left
1097 upper panel). Lighter colors - undifferentiated states; darker colors differentiating states. b)
1098 HybISS revealing the co-location of NPCs, neuronal markers and lineage-related genes
1099 revealed by trajectory analysis. c) Integrated trajectory and ST data revealing neuronal spatial
1100 differentiation. d) Spatial quantification of neuronal lineage-associated gene expression along
1101 DV axis across ages. e) UMAP indicating branches from NPCs to different glia, confirmed by
1102 RNA velocity (upper panel). f) HybISS revealing the co-location of NPCs, glial markers and
1103 lineage-related genes. g) Integrated trajectory and ST data revealing glial spatial
1104 differentiation. h) Spatial quantification of the expression of glial lineage-associated genes
1105 along DV axis across ages.

1106
1107 **Fig. 4: The regulatory networks of human spinal cord development.** a-b) Dot plots
1108 illustrating the expression of the three major signaling pathways involved in spinal cord
1109 development in different cell types (a) and their decreased expression during development (b).
1110 Max = highest expression of the given gene or module; Min = 0. c) Representative confocal
1111 images of immunostained active- β -catenin (ABC) and SHH during human spinal cord
1112 development from W5-12. d) HybISS revealing neuronal and glial progenitor patterning. e)
1113 Examples of spatial quantification of neural patterning genes along DV axis across ages. Scale
1114 bar 100 μ m. f) Circos plots displaying colocalization and major connections of different cell
1115 types during development. Solid lines: neurons; dashed lines: glia.

1116
1117 **Fig. 5: Species-specific events during neurodevelopment.** a) UMAP illustrating integrated
1118 scRNA-seq datasets of human and mouse spinal cord development. Li2022: dataset in this
1119 study. Other two datasets: publicly available mouse development datasets. b) Violin plots
1120 displaying normalized gene expression of proliferation markers *MKI67* and *TOP2A*, as well as
1121 stem cell quiescence regulator *LRIG1* during mouse and human spinal cord development. c)
1122 Representative confocal images illustrating proliferative human and mouse NPCs at early
1123 stage. Scale bar = 100 μ m. d) Violin plots displaying species difference gene expression of

1124 gliogenesis regulators. e) ST plots displaying differences of spatial gene expression of
1125 gliogenesis regulators in the developing spinal cord between human and mouse.
1126

1127 **Fig. 6: Fetal human spinal cord and relation to ependymomas.**

1128 a) ST plots displaying spinal cord tumor gene module expression. b) UMAP displaying
1129 integrated normal human spinal cord and ependymomas scRNA-seq datasets. c-e) Clusters of
1130 neuronal populations shared between conditions (c) and the expression of normal neuronal
1131 markers (d) and tumor specific markers (e). f-h) Clusters of glial populations shared between
1132 conditions (F) and the expression of normal glial markers (g) and tumor specific markers (h).
1133 i-k) Clusters of progenitor populations shared between conditions (i) and the expression of
1134 normal stem cell markers (j) and tumor specific markers (k). l-n) Trajectory analysis of EPCs-
1135 like cells (l) and lineage-associated gene expression along pseudotime (m) or among branch-
1136 related clusters (n). o-r) Trajectory analysis of ASCs-like and OPCs/OLs-like cells (o) and
1137 lineage-associated gene expression along pseudotime (p) or among branch-related clusters (q-
1138 r).
1139

1140 **Fig. 7: An integrated atlas of spinal cord cell types across rodents and humans.** a-c) UMAP
1141 illustrating the integrated spinal cord scRNA-seq dataset with cell types (a), and across datasets
1142 (b) and developmental trimesters (c). d) Dot plot illustrating cell proportions across different
1143 species, developmental stages, cell capturing chemistry and technologies.
1144

1145 **Extended Data Fig. 1. scRNA-seq reveals cell heterogeneity of the developing human**
1146 **spinal cord.** a) Quality control and filtering strategies for scRNA-seq dataset. Thick lines
1147 indicate filter thresholds. b) UMAPs identifying 47 clusters (cluster 0-46). c) Dot plot
1148 illustrating top marker genes of each cluster. In relation to Fig 1.
1149

1150 **Extended Data Fig. 2. Temporal and spatial gene expression in the developing human**
1151 **spinal cord by ST.** a) Quality control results of ST. Lines indicate filtering thresholds. b) UMAP
1152 illustrating 23 clusters from 76 ST sections at W5, W8, W9 and W12. C) Representative
1153 sections of ST spatial maps of all clusters along rostral-caudal axis. R = rostral, C = caudal. D)
1154 Dot plot illustrating the top marker genes for all clusters in the ST analysis. e) Bar graph
1155 illustrating cell type proportions across sections along rostral-caudal axis. In relation to Fig 1.
1156

1157 **Extended Data Fig. 3. Stereoscope revealing integrated results of scRNA-seq and ST.**
1158 Representative stereoscope images revealing cell type positions and their probability along the
1159 rostral-caudal axis at W5, 8, 9 and 12. R = rostral, C = caudal. Intermediate neuronal
1160 progenitors (INPs), excitatory neurons (ExNs), inhibitory neurons (IbNs), cholinergic neurons
1161 (ChNs), astrocytes (ASCs), ependymal cells (EPCs), oligodendrocyte precursor cells (OPCs),
1162 oligodendrocytes (OLs). In relation to Fig 1.
1163

1164 **Extended Data Fig. 4. Validation of cell populations, cell fate commitment and neural**
1165 **patterning at early developmental stage.** a-g) Representative IHC images illustrating
1166 localization of ExNs, IbNs and ChNs (a-b), ASCs (c) and OPCs (d) in W8 human spinal cord
1167 as well as SHH and Notch related proteins at W5 human spinal cord sections (e-g). h)
1168 Representative HybISS images illustrating early glial cells at W8. Rectangles indicating
1169 enlarged areas. i) Representative HybISS images illustrating localization of subpopulations of
1170 IbNs, OPCs and OLs during human spinal cord development. Scale bars: 100 μ m. In relation
1171 to Fig 2 and Fig 4.
1172

1173 **Extended Data Fig. 5. Locolization of heterogenous cell types or cell states of neural cells**
1174 **in the human developing spinal cord.** Representative images from stereoscope analysis
1175 illustrating the probability of spatial distribution of each cell subpopulation or cell state of the
1176 major neural cells at W8. In relation to Fig 2.
1177

1178 **Extended Data Fig. 6. Heterogenous NPCs with different activeness in the developing**
1179 **human spinal cord.** a) Dot plot illustrating the top markers for the NPC clusters. b-c) Violin
1180 plots illustrating stem cell markers (b) and cell cycle scores (c) of human NPCs across clusters
1181 and ages. d) Stereoscope illustrating the probability of spatial distribution of different NPCs in
1182 the developing human spinal cord sections. e) HybISS illustrating the locations of the
1183 proliferative NPC clusters from W5-12. Scale bar 100 μ m. f) UMAP illustrating integrated
1184 datasets and subtypes of NPCs. g) Violin plots illustrating consistent results for gene expression
1185 of proliferation markers and subtype specific markers in the integrated dataset. h) Top GO
1186 terms of early non-proliferative NPCs compared to proliferative NPCs. In relation to Fig 2-3.
1187

1188 **Extended Data Fig. 7. Cell fate commitment of hNPCs during human spinal cord**
1189 **development.** a) UMAP showing strong connectivity of different NPC clusters during
1190 development. b) scVelo analysis revealing the predicted differentiation trajectory from
1191 proliferative NPCs to neuronal and glial fate committed NPCs. c-d) Hierarchical tree from
1192 URD analysis displaying NPC trajectory during development. e) Hierarchical trees illustrating
1193 examples of top genes associated with neuronal and glial lineage during cell fate commitment
1194 of hNPCs. In relation to Fig 3.
1195

1196 **Extended Data Fig. 8. Spatiotemporal regulation of human neurogenesis and gliogenesis.**
1197 a-b) Hierarchical trees from URD analysis displaying neurogenesis and gliogenesis (a) as well
1198 as top lineage-associated genes (b) during human spinal cord development. c) Representative
1199 HybISS images illustrating the co-locolization of NPC markers, committed cell fate markers
1200 and lineage-associated genes. Scale bar 100 μ m. e) ST plots illustrating the spatial expression
1201 of top lineage genes revealed by scRNA-seq. In relation to Fig 3.
1202

1203 **Extended Data Fig. 9. Lineage associated regulons have species difference during**
1204 **neurodevelopment.** a-b) Dot plots illustrating top regulons (a) and their gene expression (b)
1205 in human major cell types during development. c) Dot plot illustrating top regulons during
1206 mouse spinal cord development. d) Dot plots illustrating top regulons and their gene expression
1207 during human neurogenesis and gliogenesis. In relation to Fig 5.
1208

1209 **Extended Data Fig. 10. Neural patterning gene expression in the early developmental**
1210 **human spinal cord.** Neural patterning genes related to progenitor and postmitotic neurons are
1211 plotted in W5 and W8 representative human spinal cord sections along the dorsal-ventral axis.
1212 Most of the neural patterning genes enriched in the progenitors appear at W5 but most of them
1213 disappear at W8 (Left panel). In contrast, neural patterning genes expressed in neurons are
1214 mostly absent at W5 but exhibit a dorsal-ventral patterns at W8. In relation to Fig 4.
1215

1216 **Supplementary Figure 1. Selection of probes for HybISS based on major cell type**
1217 **markers.** Dot plot illustrating the correlation between major cell types from scRNA-seq and
1218 the chosen probes for validation with HybISS.
1219

1220 **Supplementary Figure 2. Selection of probes for HybISS based on subpopulations of each**
1221 **major cell type markers.** Dot plot illustrating the correlation between subtypes or cell states
1222 within each major cell type from scRNA-seq and the chosen probes for validation with HybISS.

1223

1224 **Supplementary Figure 3. Spatiotemporal gene expression regulates neurogenesis and**
1225 **gliogenesis.** a) Dot plot illustrating different markers among three lineages of IbNs. b) GO
1226 terms of three terminal clusters of IbNs. c) Minimal spanning tree (MST) displaying the
1227 strongest connections between clusters related to neurogenesis. d) Heatmaps illustrating
1228 lineage differential gene expression of each branch. e) MST displaying the strongest
1229 connections between clusters related to gliogenesis. f) Heatmaps illustrating lineage
1230 differential gene expression of each branch.

1231

1232 **Supplementary Figure 4. The regulatory networks of human spinal cord development.** a)
1233 Dot plot illustrating the expression of signaling pathway genes in all major cell types
1234 throughout W5-12 developmental stages. b) Interactome analysis indicate the interaction
1235 between every two cell types and the ligands and receptors contributing to the interactions. L
1236 = ligand, R = receptor. Red lines indicate increased expression of related ligands or receptors,
1237 while blue lines indicate decreased expression of related ligands and receptors during
1238 development. Thicker lines between ligands and receptors indicate higher probability of
1239 connections and cell-cell interactions.

1240

1241 **Supplementary Figure 5. Top regulons during human and mouse spinal cord**
1242 **development.** a) Dot plot illustrating the most significant regulons in the developing human
1243 spinal cord during W5-12 across major cell types and age. b) Dot plot illustrating the most
1244 significant regulons in the developing mouse spinal cord from E9.5-P11 across major cell types
1245 and age.

1246

1247 **Supplementary Figure 6. Fetal human spinal cord and relation to ependymomas.** a)
1248 UMAP displaying all major cell types revealed by the integrated scRNA-seq dataset of human
1249 developing spinal cord and human ependymomas. b) Heatmaps revealing the most significantly
1250 differential expressed genes in two lineages of EPCs-like cells and ASCs and OPCs/OLs-like
1251 cells during trajectory analysis. c) Dot plot illustrating the expression of putative cancer stem
1252 cell marker genes across all subtypes of human NPCs and human CSCs and is selectively
1253 enriched in cluster 3, 6, and 7.

1254

1255 **Supplementary Figure 7. Correlation with annotations from previous spinal cord**
1256 **datasets.** Heatmaps illustrating good correlation between the annotation of scRNA-seq data
1257 from this study with previous scRNA-seq data by two different correlation calculations.

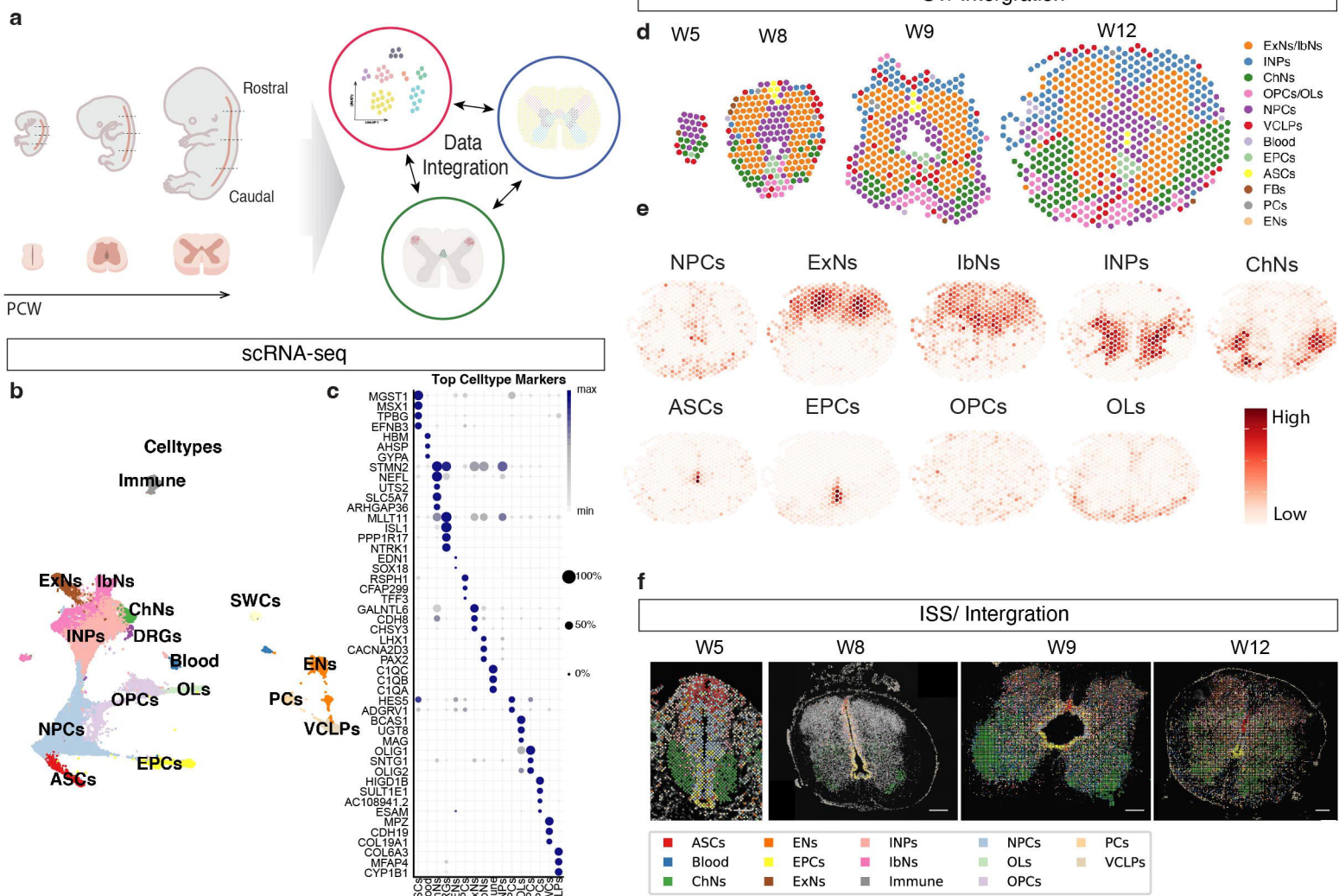
Figure 1.

Figure 2

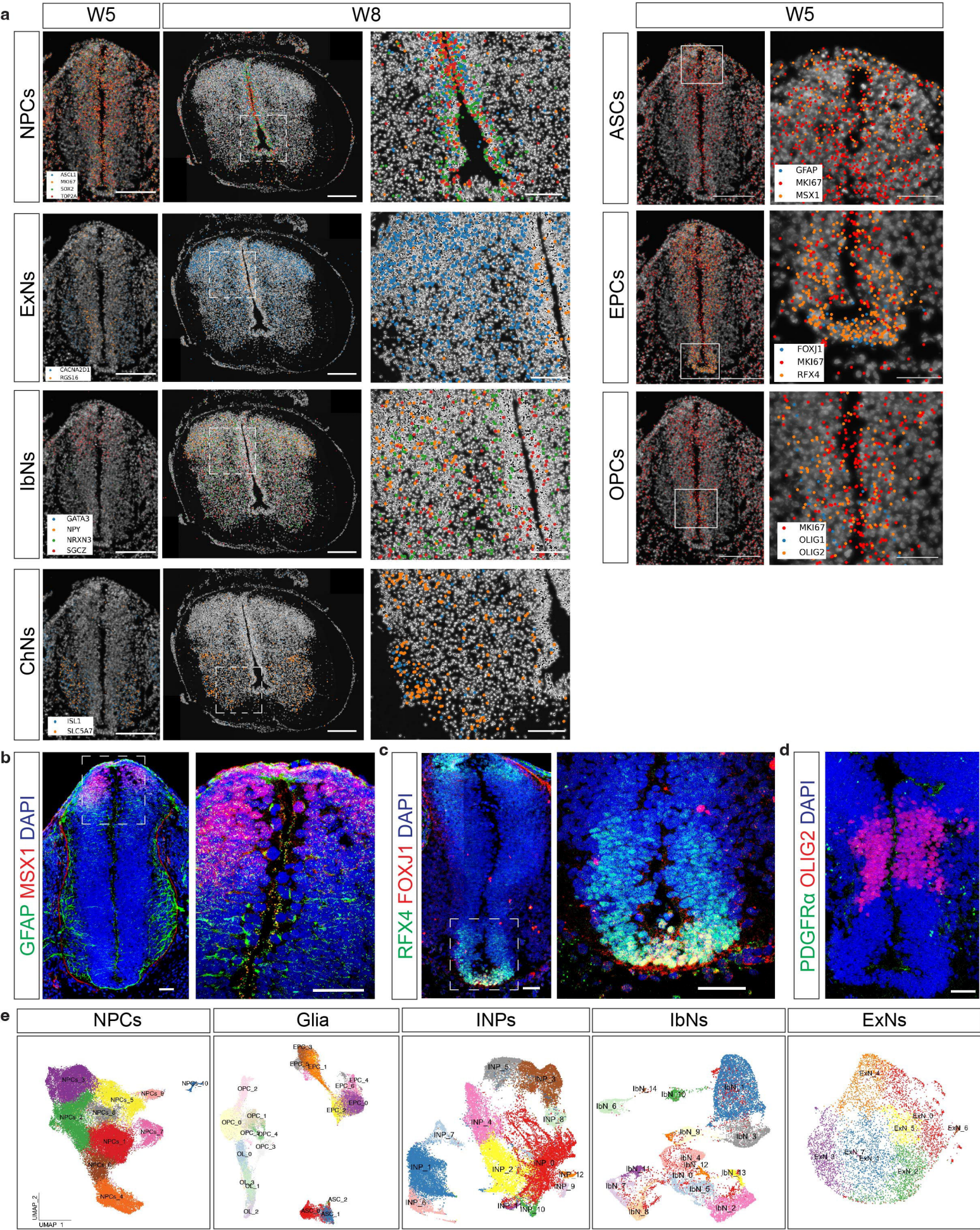


Figure 3.

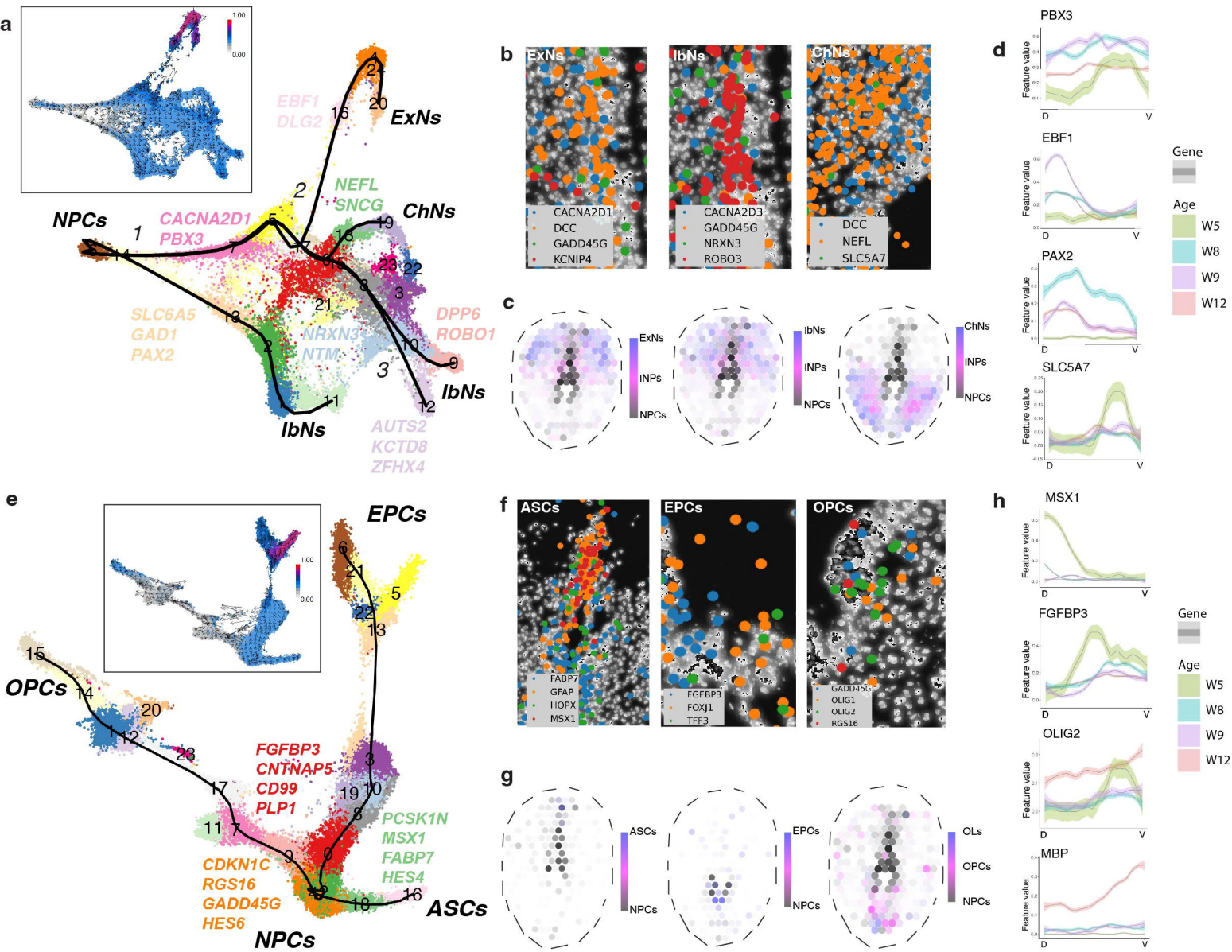


Figure 4.

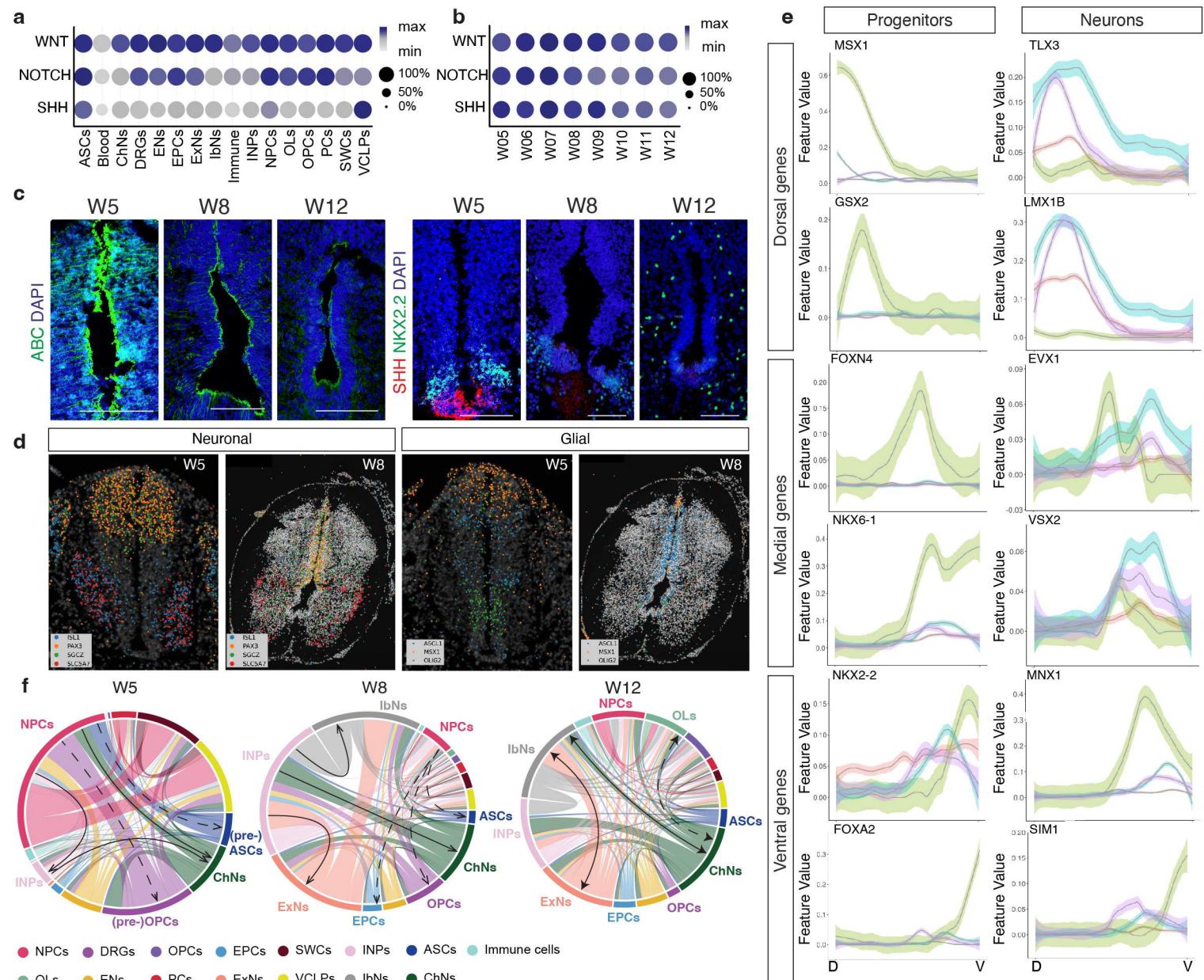


Figure 5.

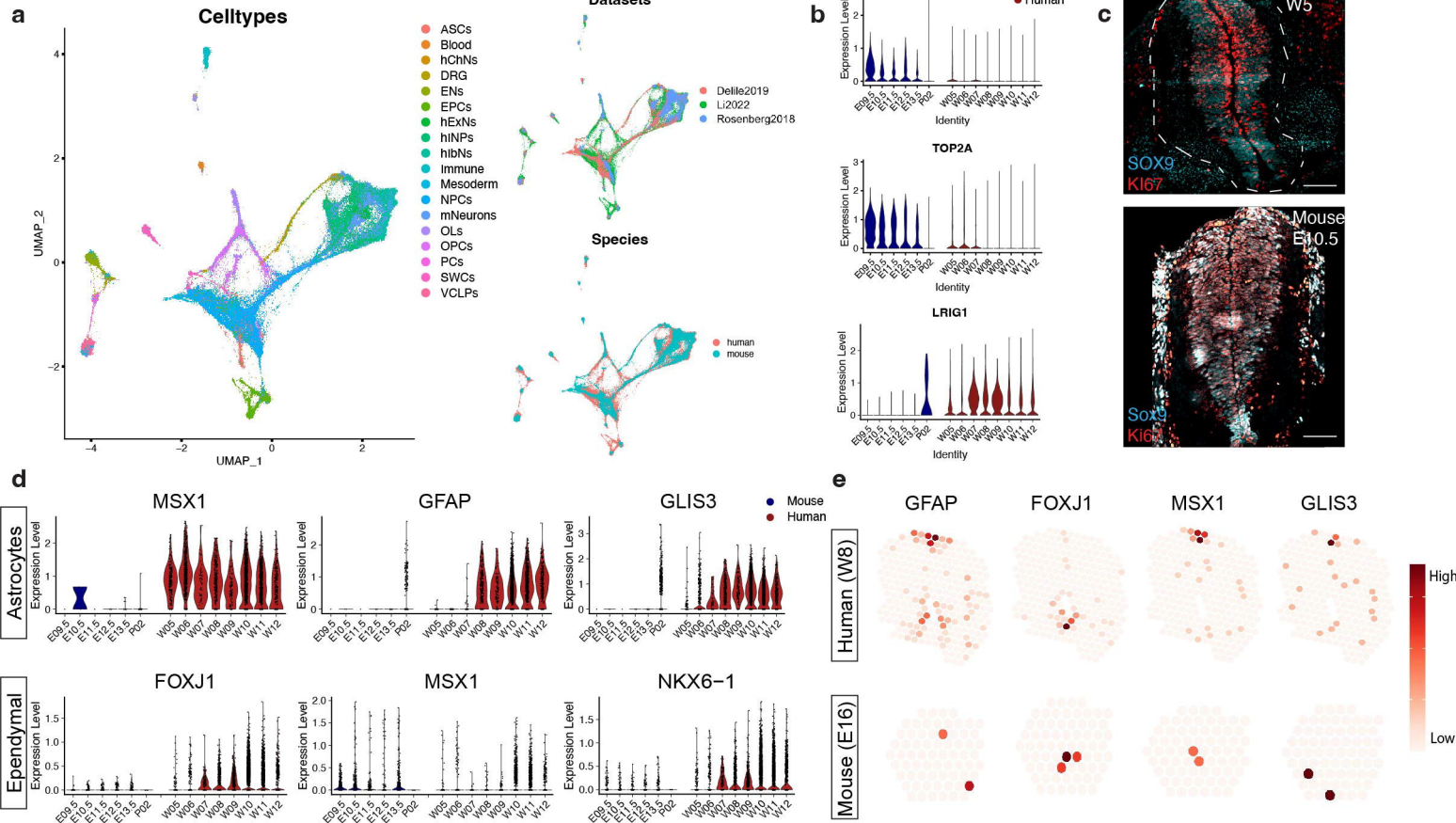
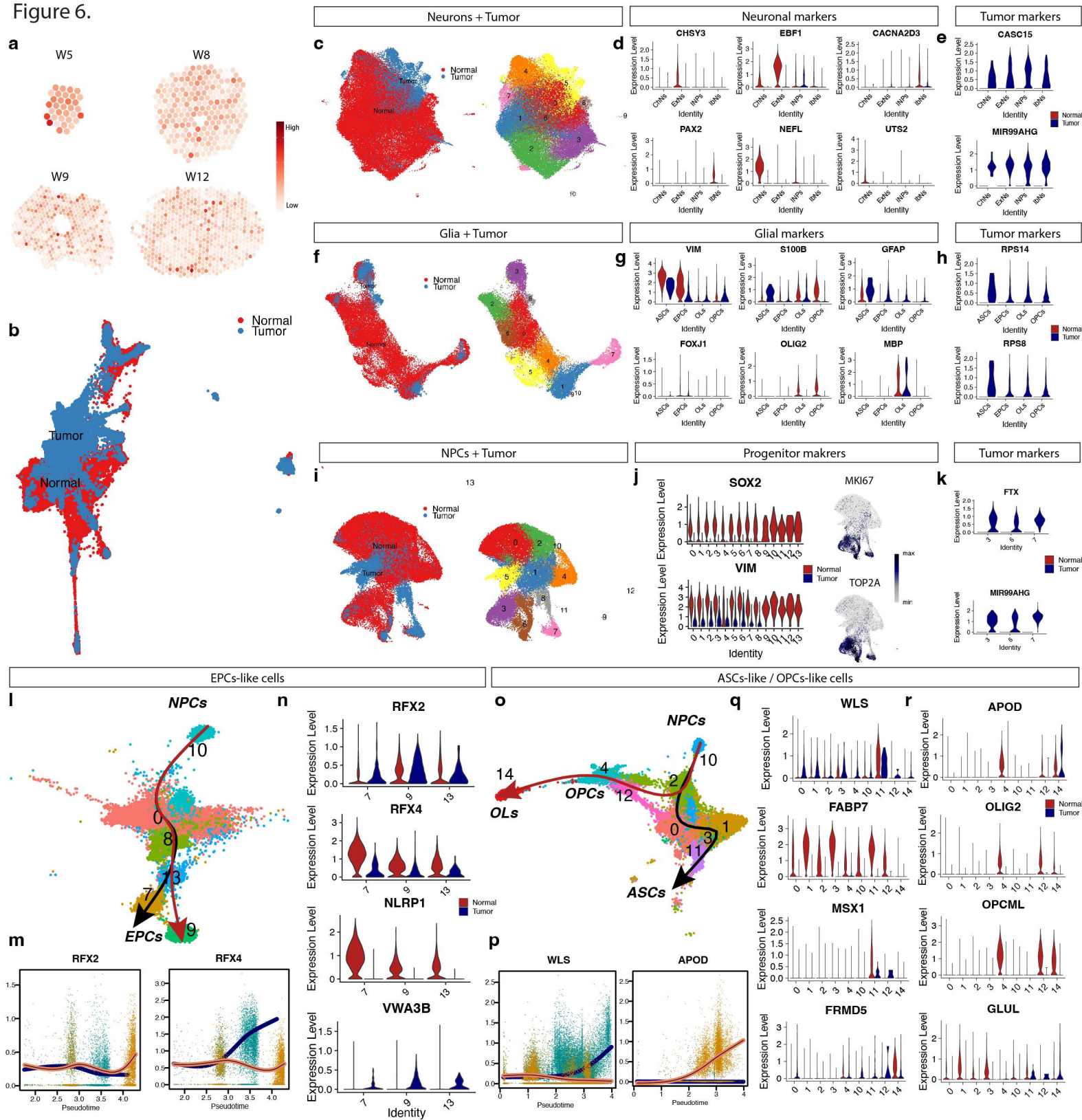
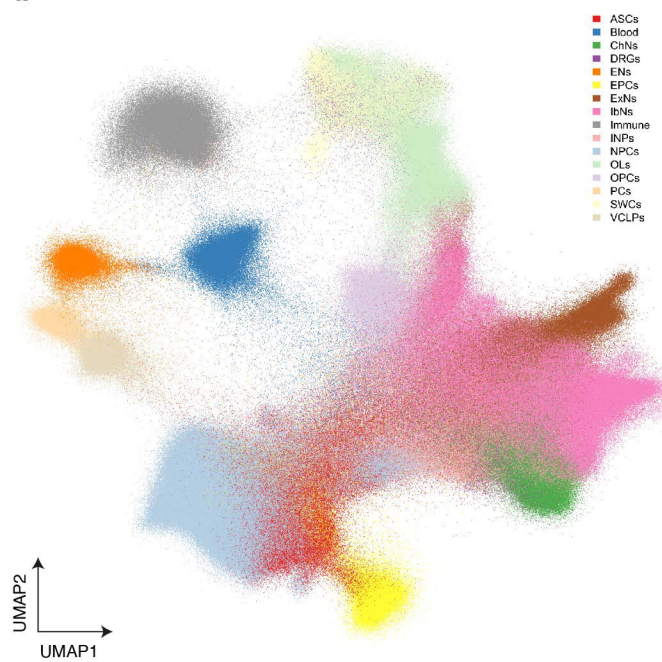
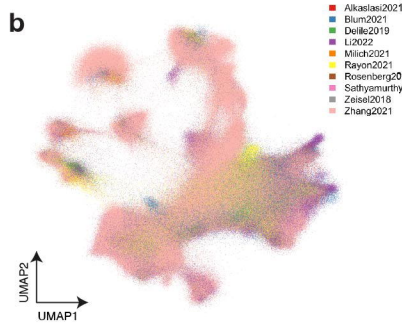
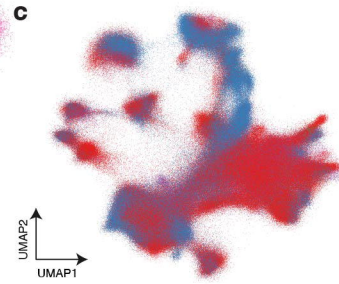
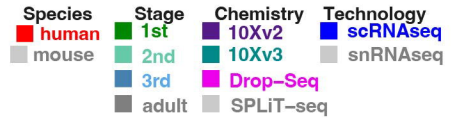
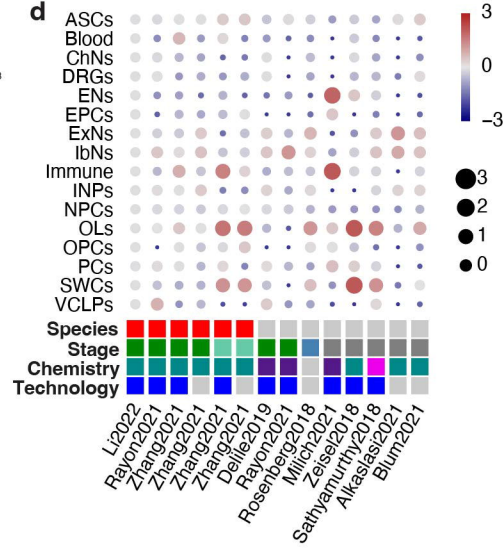
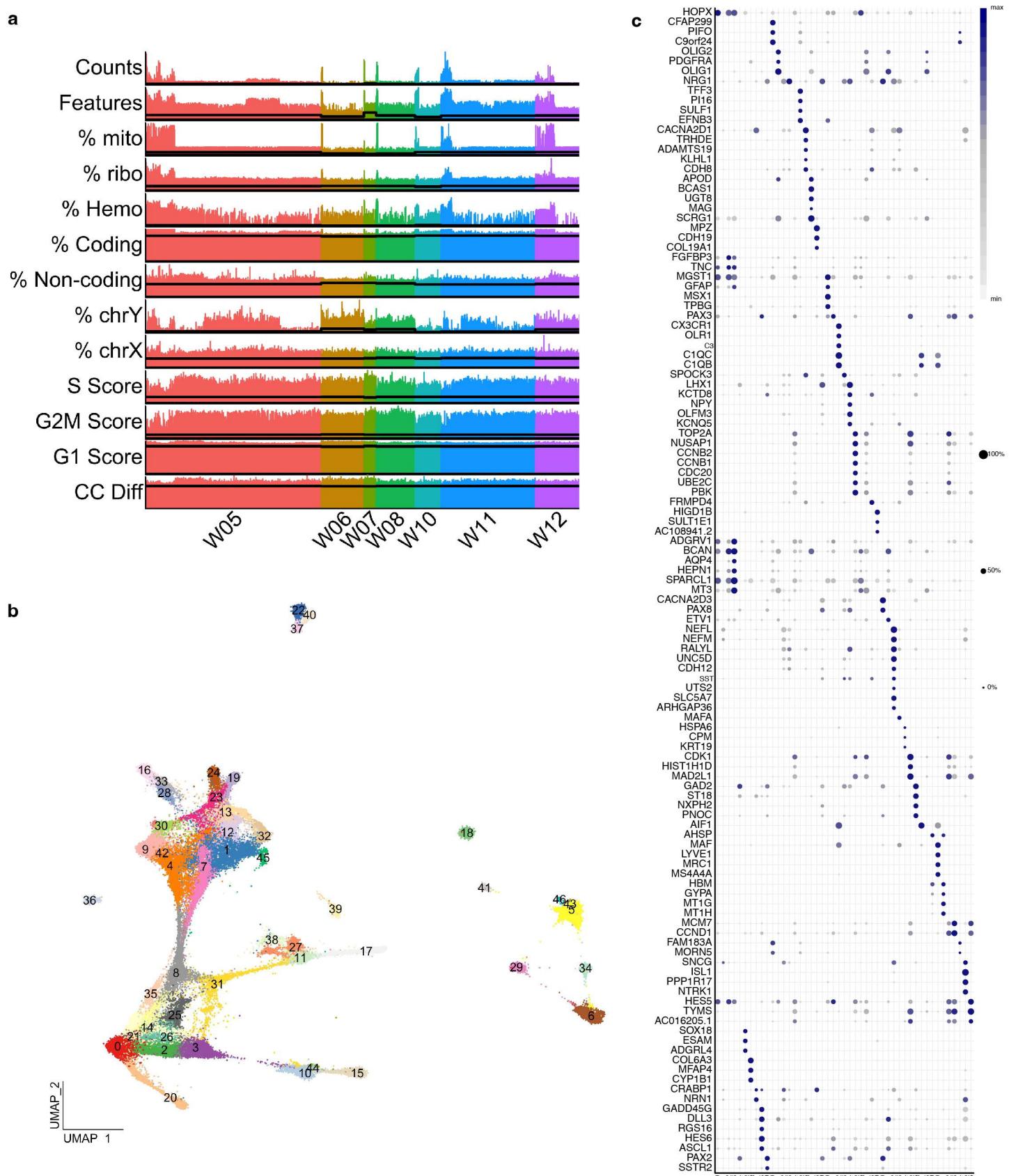


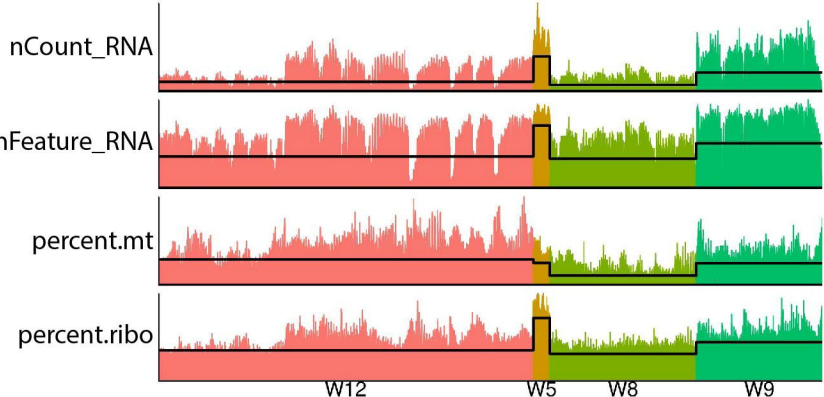
Figure 6.

a**b****c****d**

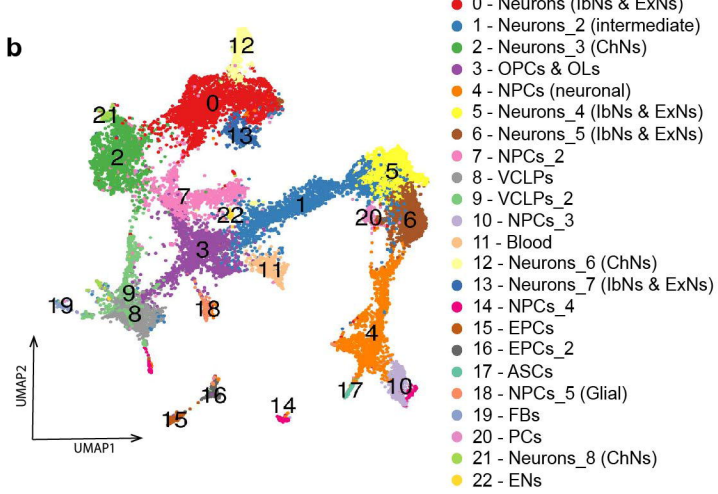
Extended Data Figure 1



a



b



c

R → C

W5



W8



W9

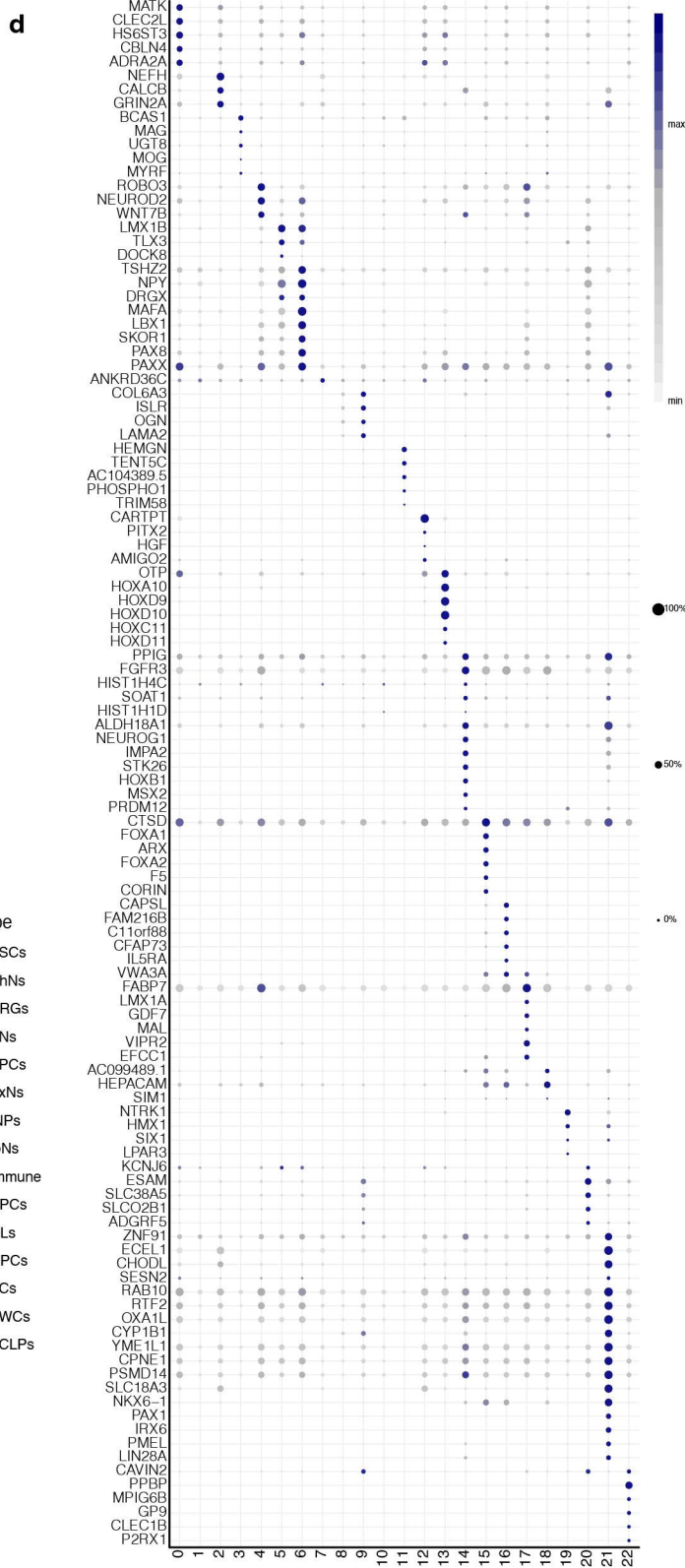


W12



e

d



percent

celltype

ASCs

ChNs

DRGs

ENs

EPCs

ExNs

INPs

IbNs

Immune

NPCs

OLs

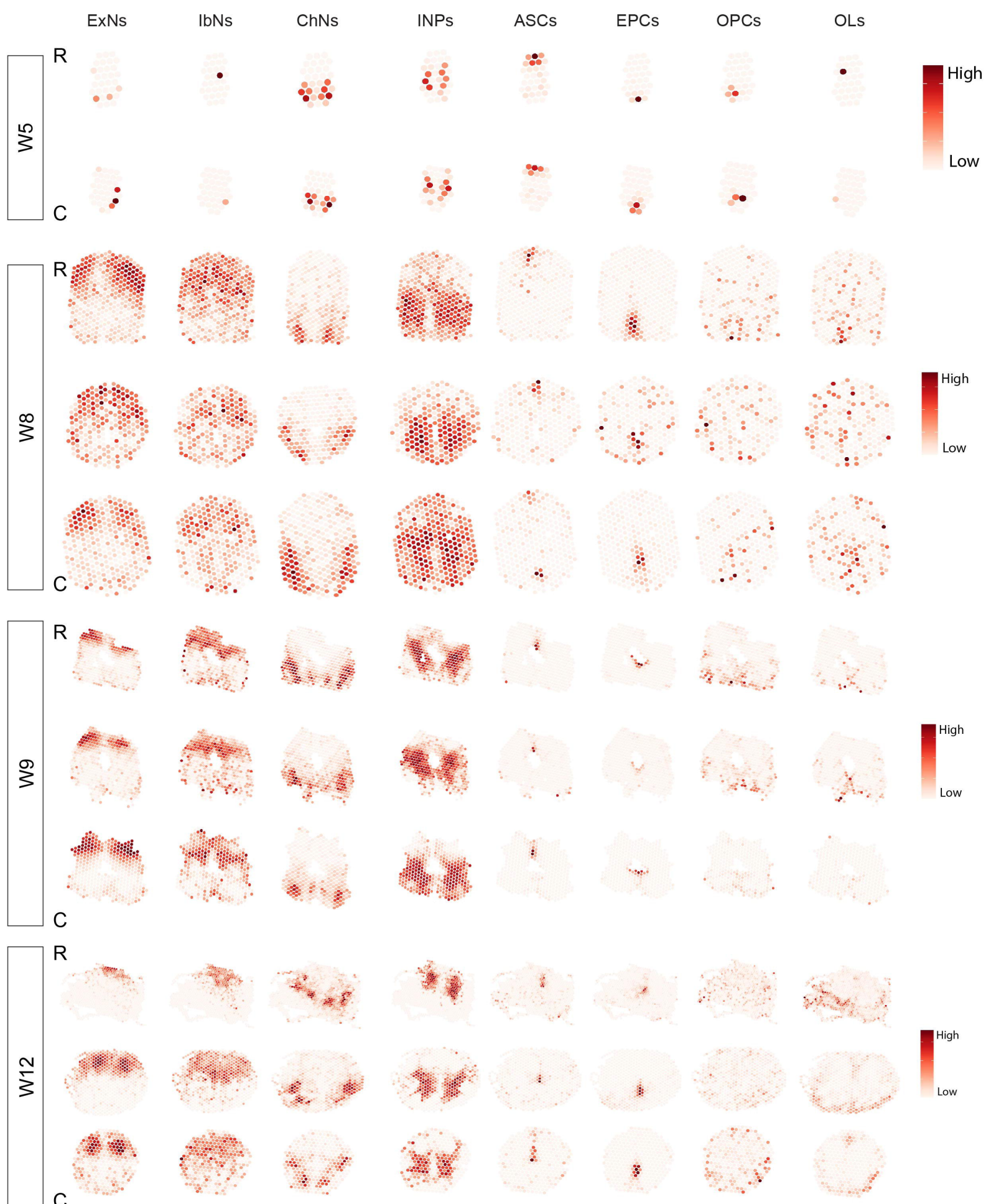
OPCs

PCs

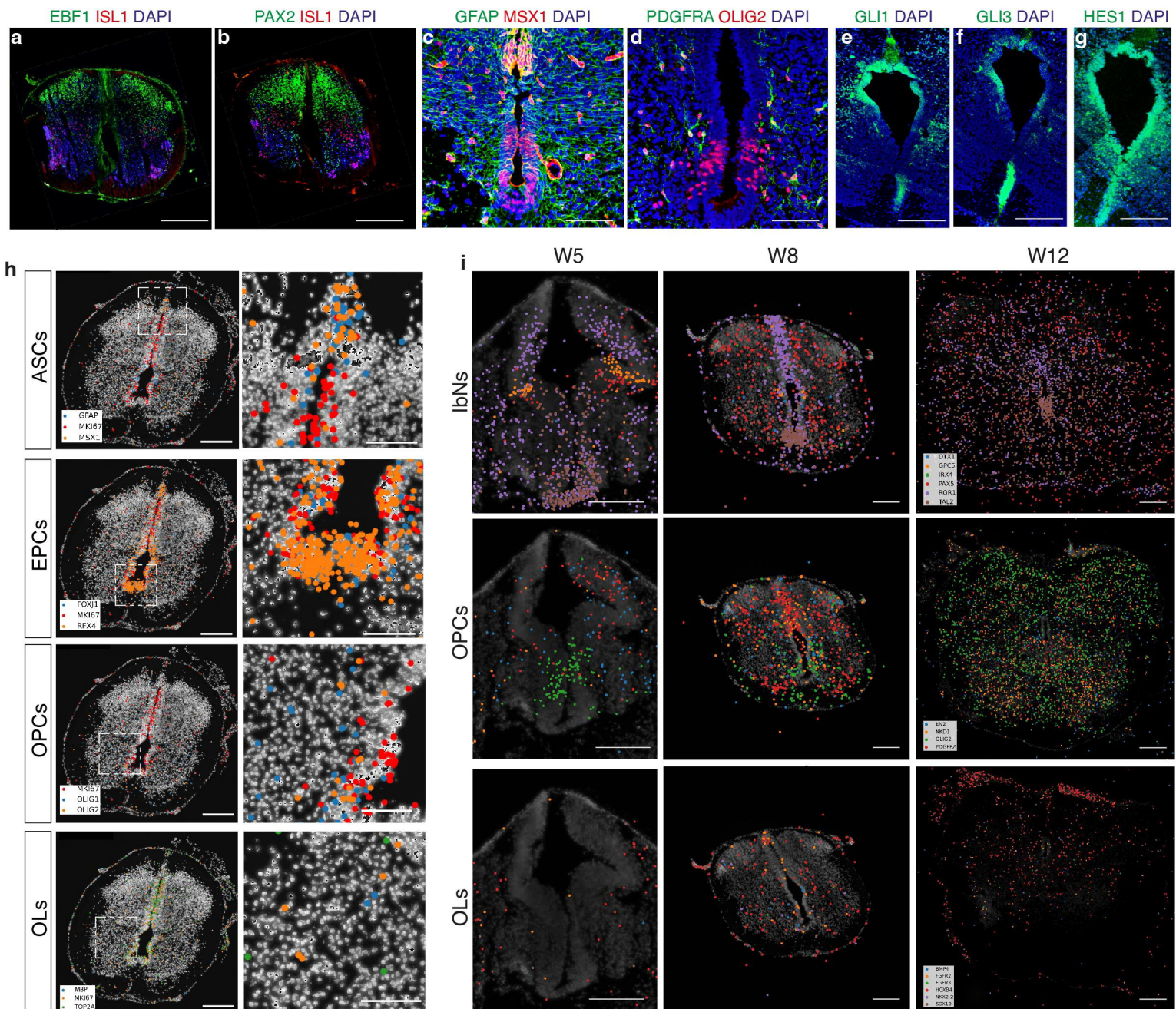
SWCs

VCLPs

Extended Data Figure 8

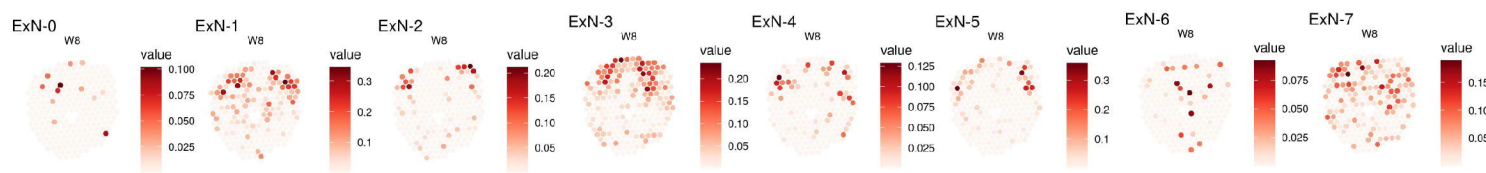


Extended Data Figure 4

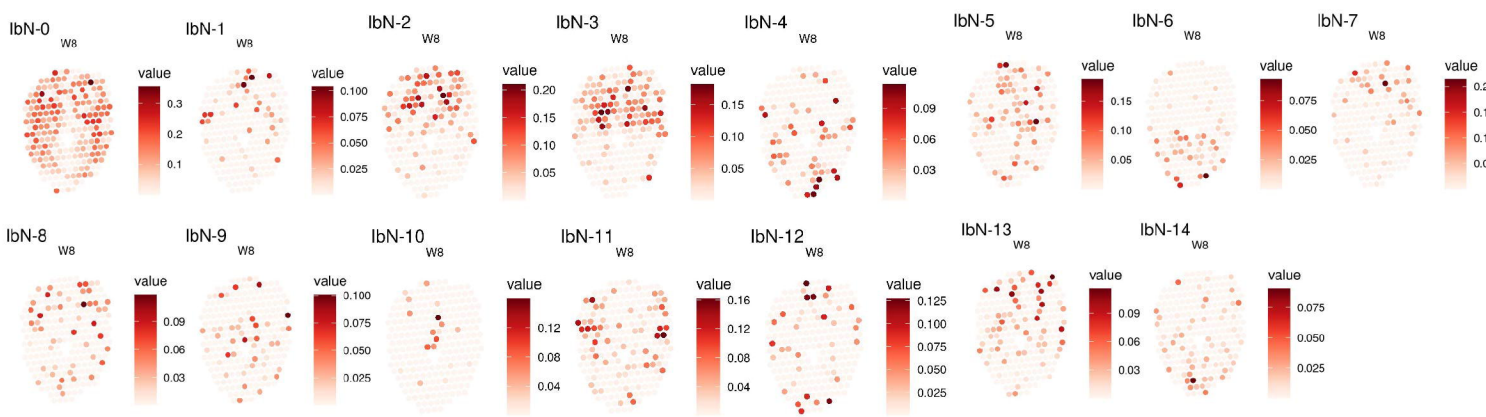


Extended Data Figure 5

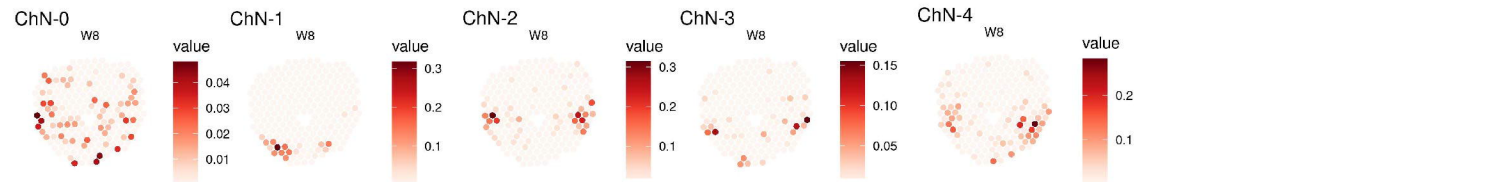
ExNs



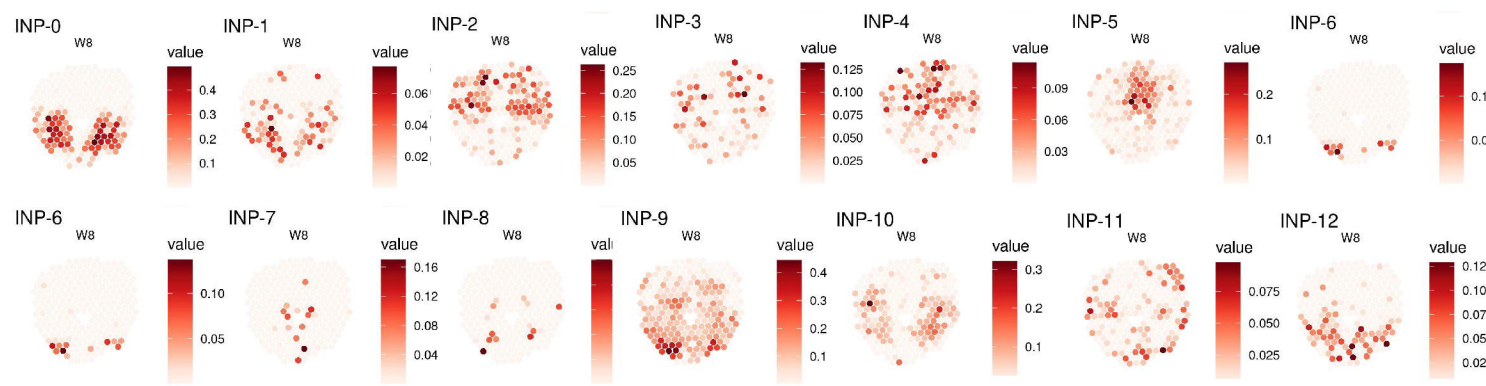
IbNs



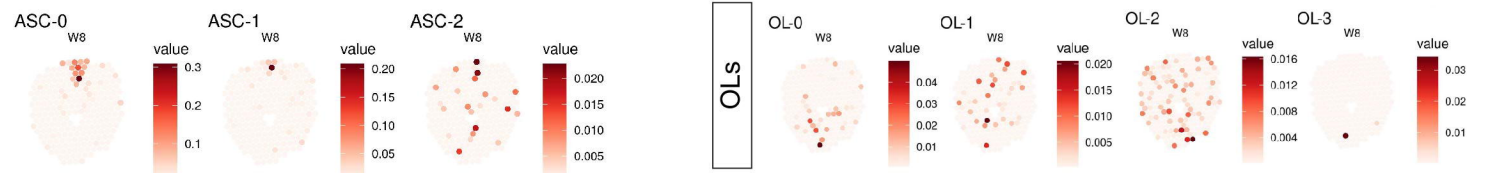
ChNs



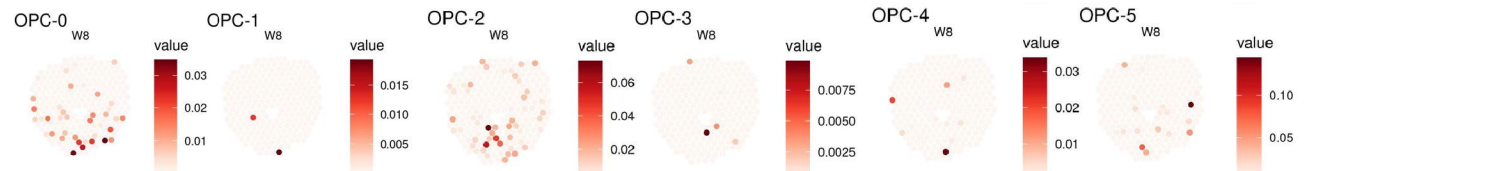
INPs



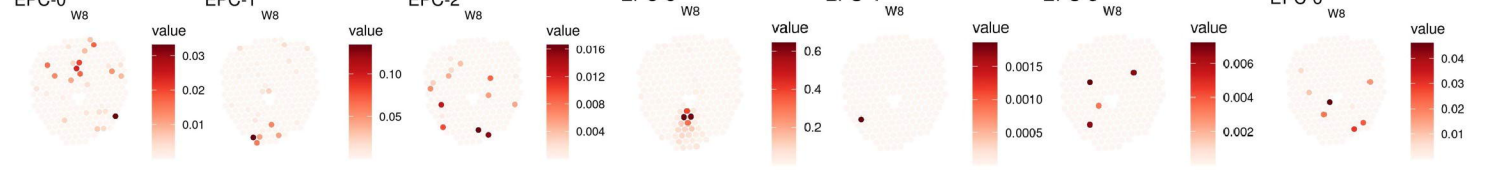
ASCs



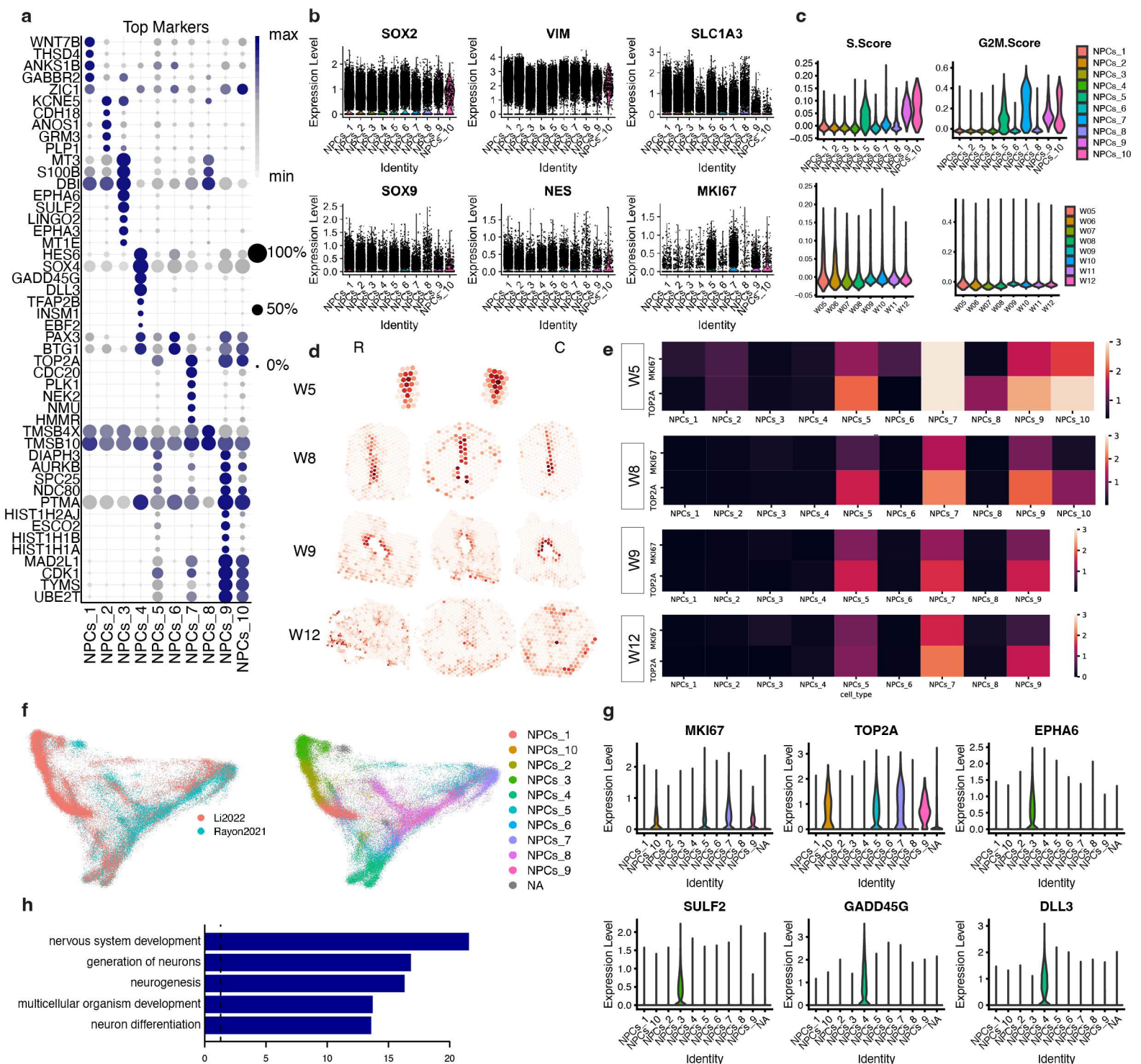
OPCs



EPCs

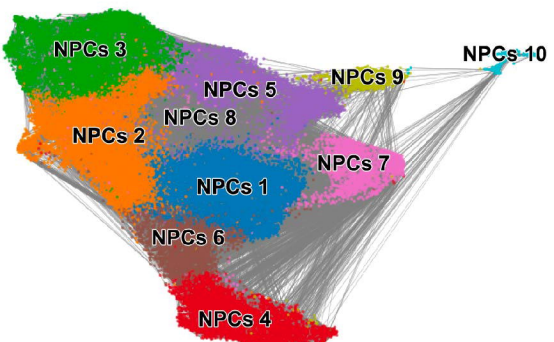


Extended Data Figure 6

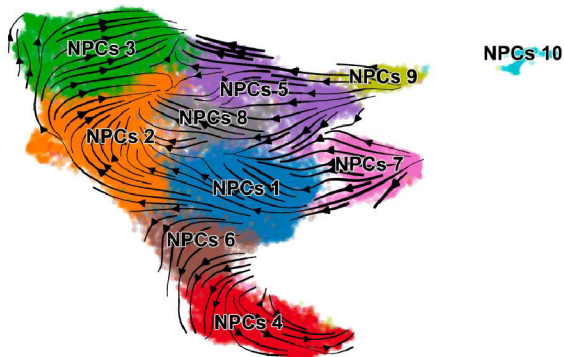


Extended Data Figure 7

a

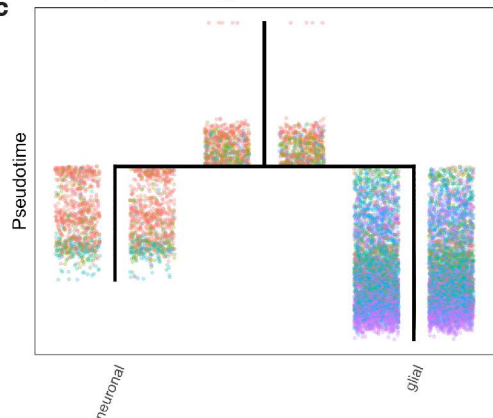


b

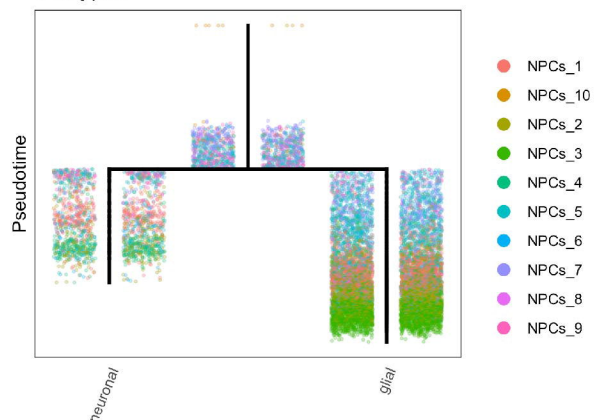


Developmental Stage

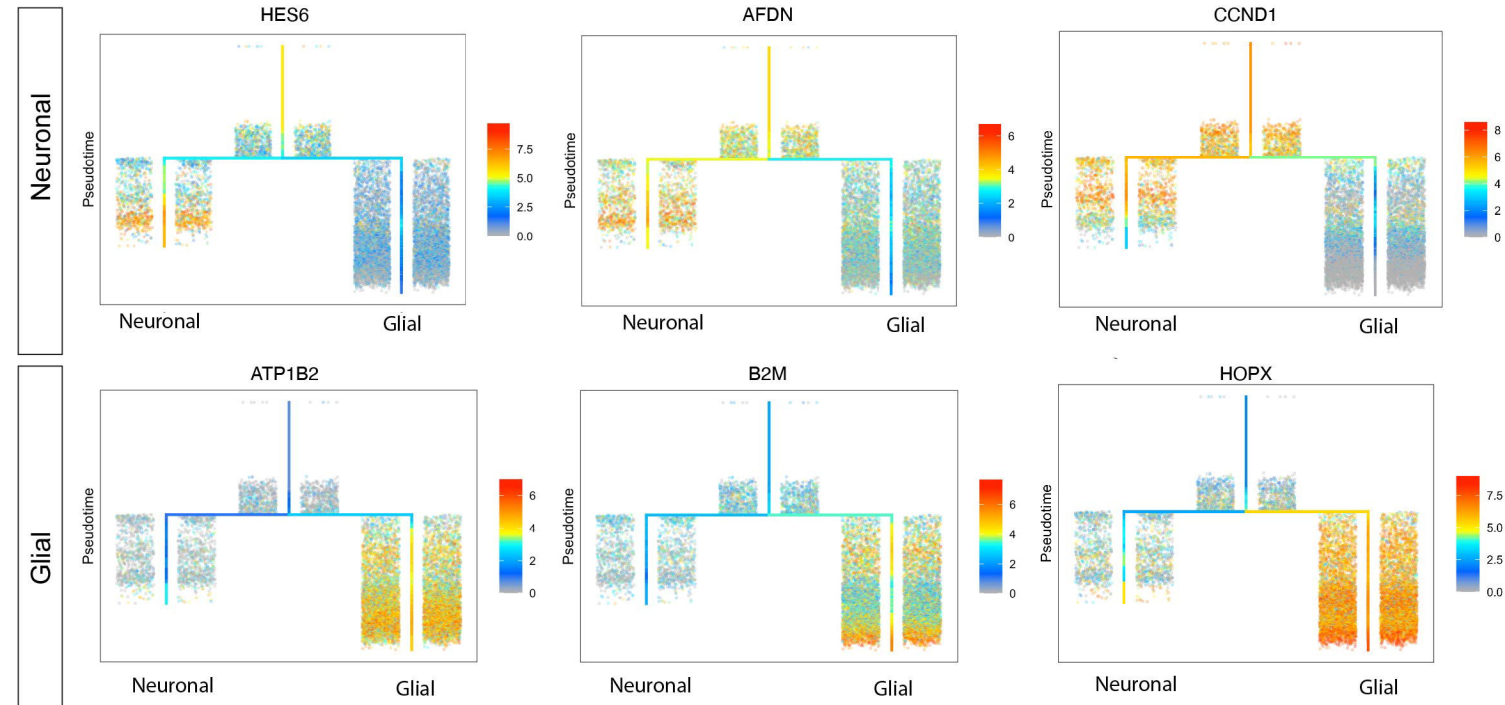
c



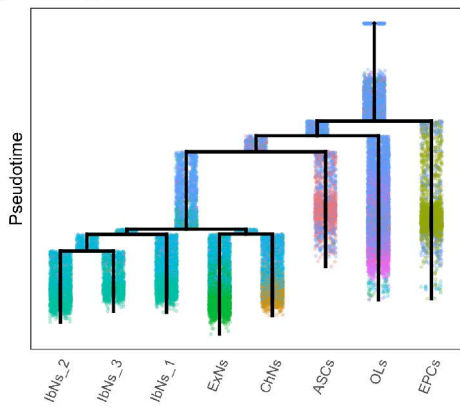
d Subtypes



e

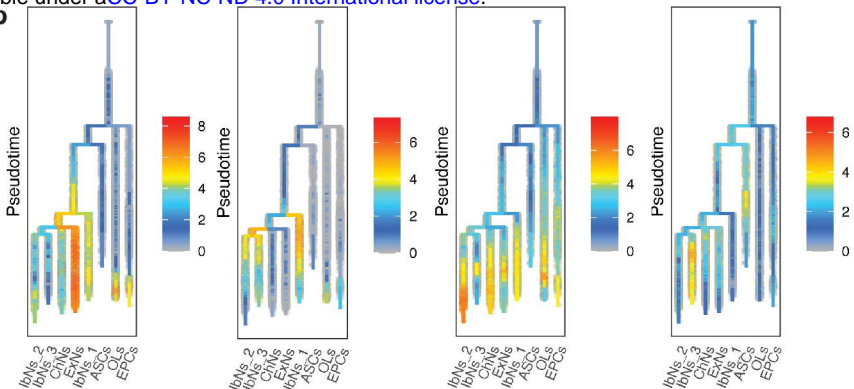


a Cell Types



ASCs
ChNs
EPCs
ExNs
IbNs
INPs
NPCs
OLs
OPCs

b



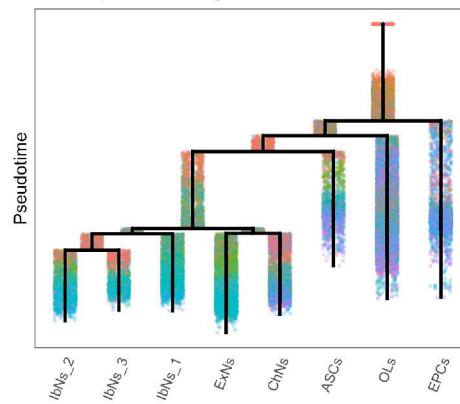
NEFL

MSX1

NTN1

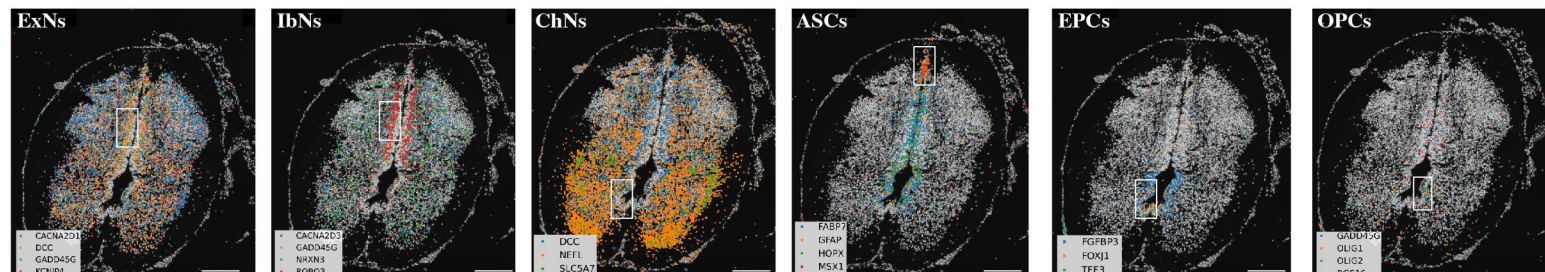
OLIG2

Developmental Stage

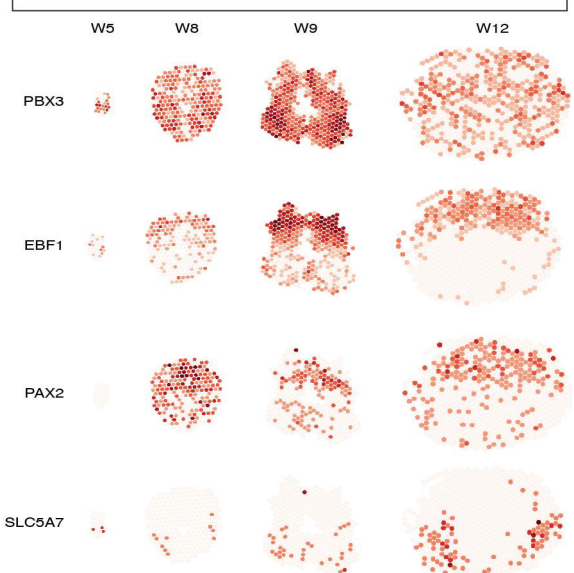


W05
W06
W07
W08
W09
W10
W11
W12

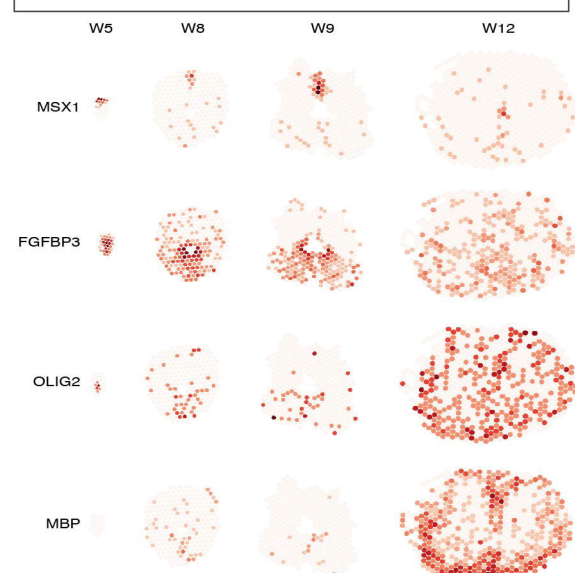
c



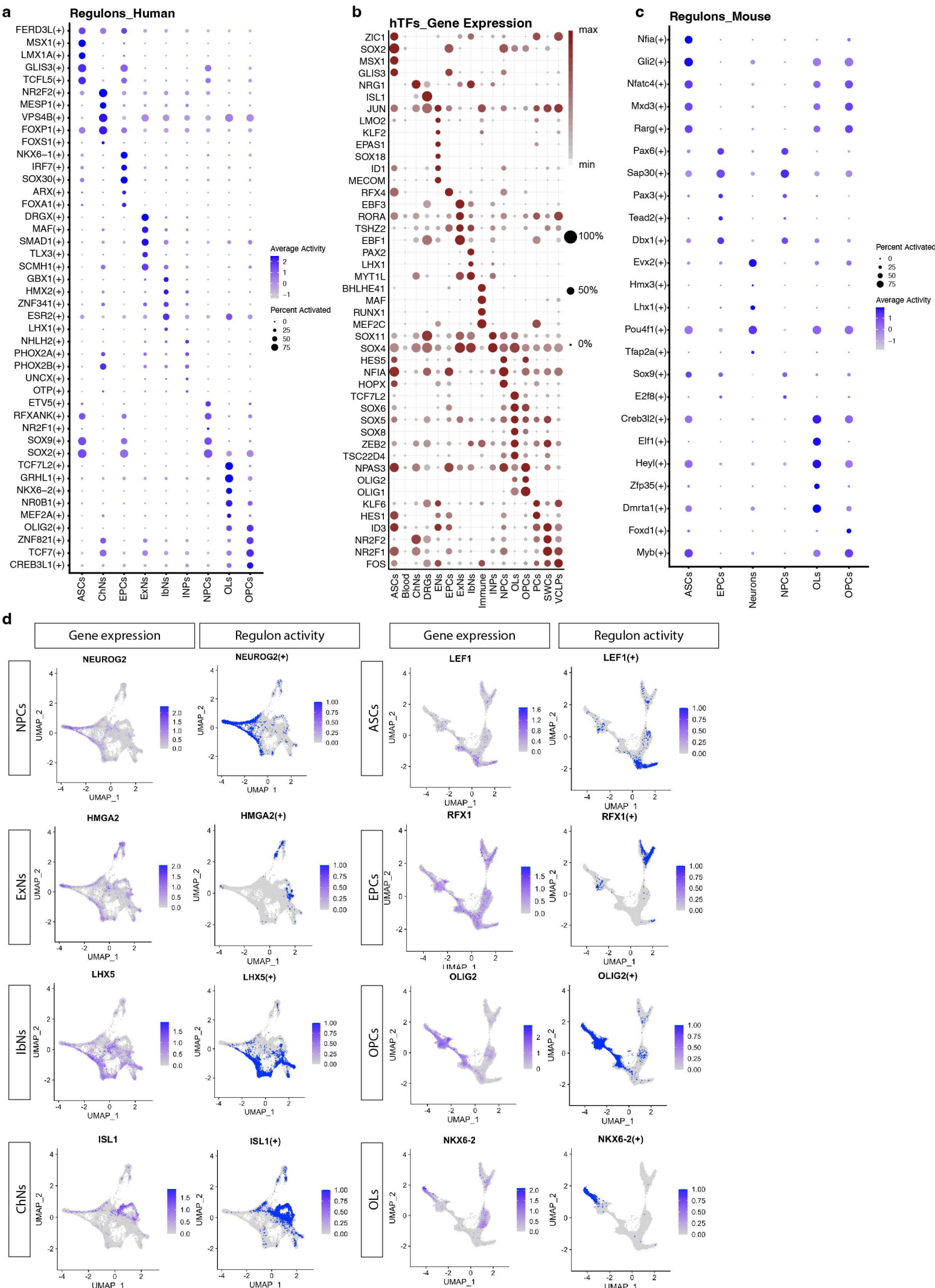
d Neurogenesis



e Gliogenesis



Extended Data Figure 9



Extended Data Figure 10

